

Bifurcation analysis of a two-neuron central pattern generator model for both oscillatory and convergent neuronal activities

Kotaro Muramatsu¹ and Hiroshi Kori^{1,2}

¹*Department of Mathematical Informatics, Graduate School of Information Science and Technology, The University of Tokyo, Japan*

²*Department of Complexity Science and Engineering, Graduate School of Frontier Sciences, The University of Tokyo, Japan*

(*Electronic mail: oratok-m@g.ecc.u-tokyo.ac.jp, kori@k.u-tokyo.ac.jp)

The neural oscillator model proposed by Matsuoka is a piecewise affine system, which exhibits distinctive periodic solutions. Although such typical oscillation patterns have been widely studied, little is understood about the dynamics of convergence to certain fixed points and bifurcations between the periodic orbits and fixed points in this model. We performed fixed point analysis on a two-neuron version of the Matsuoka oscillator model, the result of which explains the mechanism of oscillation and the discontinuity-induced bifurcations such as subcritical/supercritical Hopf-like, homoclinic-like, and grazing bifurcations. Furthermore, it provided theoretical predictions concerning a logarithmic oscillation-period scaling law and noise-induced oscillations, which are both observed around those bifurcations. These results are expected to underpin further investigations into both oscillatory and transient neuronal activities with respect to central pattern generators.

The Matsuoka oscillator model is a neuronal network model, which exhibits oscillatory activities owing to the adaptation property of each neuron and the mutual inhibitions between neurons. This is often applied to modeling the spinal oscillatory neuronal circuits known as central pattern generators (CPGs) and for simulating biological locomotion such as human bipedal walking. However, most previous studies have overlooked its dynamics that converge toward stationary states, corresponding to transient neuronal activities and non-oscillatory movements. In this study, we conducted fixed point analysis on a two-neuron case of the Matsuoka oscillator model. We (I) formulated the existence and stability of all possible fixed points, (II) demonstrated the emergence of oscillatory solutions and bifurcation mechanisms between oscillatory and convergent dynamics, and (III) predicted a logarithmic oscillation-period scaling law and noise-induced oscillation. Our results indicate that central nervous systems might take advantage of CPGs for rhythmic locomotion and non-oscillatory or discrete movements. The discussion of limitations presented herein will, in the future, probably be followed by extending the Matsuoka oscillator model to understand an integrative mechanism for neural control of both rhythmic and discrete movements.

I. INTRODUCTION

A biological neural circuit, CPG, is the basis of rhythmic movements, e.g., locomotion and respiration, in animals.^{1,2} The CPGs of vertebrates are located in the spinal cord. Furthermore, CPGs can generate stable oscillatory activities by receiving stationary inputs or tonic drives descending from a part of the brainstem, the mesencephalic locomotor region (MLR). The CPGs oscillation patterns are also modulated by feedback from peripheral sensory organs, contributing to highly autonomous and adaptive motor control. Recent studies have suggested that the spinal interneuronal networks thought to implement CPGs are also involved in discrete, transient, non-oscillatory movements such as point-to-point reaching with the upper limbs.³⁻⁵

Various dynamical system models mathematically describe the CPG functions. The Matsuoka oscillator model, which focuses on the dynamics of neuronal firing rates, is an example.⁶⁻⁸ Despite having less precise temporal resolution than spiking neuronal network models,⁹ firing rate models are useful for understanding neural phenomena in macroscopic timescales such as neuromuscular activity and motor control. Thus, the Matsuoka oscillator model has been applied to the simulation

studies of human bipedal walking.¹⁰⁻¹² Additionally, the physiological interpretation of the model is feasible, compared to more abstract models without neuronal configuration such as the phase oscillator model.¹ The Wilson-Cowan model^{13,14} is another firing rate model, although it addresses neither the adaptation properties nor the mutual inhibitory connections of neurons. In particular, the latter feature follows the half-center structure of spinal circuits,² which validates the Matsuoka oscillator as a basic hypothetical model for CPGs.

For dynamical systems, rhythmic oscillatory activities are represented as stable limit cycles in the Matsuoka oscillator model. The original paper on this model (Ref. 6) presents several proofs for the existence condition of oscillatory solutions. However, previous studies have mainly focused only on its distinctive oscillatory solutions,¹⁵ whereas some transient activities with convergence to stationary states or fixed points have been insufficiently discussed. Ref. 16 highlighted this problem; however, the terminal stationary states are not realized by positive constant inputs and positive neuronal inner states. Furthermore, little is known and understood on the bifurcation types, mechanisms, and critical behaviors in the vicinity of the bifurcations that emerge between such fixed points and the well-known limit cycles. Therefore, further investigation into attracting fixed points and their relevant bifurcations is essential for grasping the possibility of transient activities in the Matsuoka oscillator model, which could be related to discrete, transient movements.

This study mainly aims to systematically formulate possible fixed points corresponding to stationary states that appear in the Matsuoka oscillator model and to investigate bifurcations between oscillatory solutions and fixed points in addition to the oscillation mechanism. We first review the original Matsuoka oscillator model (Section II); thereafter, we discuss the classification of oscillation types and approximations of the oscillation period (Section III). This review is followed by a comprehensive fixed point analysis regarding the existence and stability of fixed points (Section IV). Based on the analysis results, we present theoretical formulations to explain the emergence of oscillations and bifurcation scenarios (Section V). A logarithmic oscillation-period scaling law and a novel prediction of noise-induced oscillations are also proposed. Throughout this paper, we attempt to provide a foundation for understanding the common mechanisms underlying the oscillatory and convergent neuronal activities that both emerge in one of the well-known CPG models.

II. BASIS OF THE STUDY

A. The Matsuoka Oscillator Model

The Matsuoka oscillator model⁶⁻⁸ is a neural oscillator model comprising n firing neurons with neuronal adaptation properties and mutual inhibitions. The time evolution of the i -th neuron (the neuron- i) is described using the following differential equations:

$$\tau_x \frac{dx_i}{dt} = -x_i - by_i - \sum_{j \neq i}^n a_{ij} z_j + s_i, \quad (1a)$$

$$\tau_y \frac{dy_i}{dt} = -y_i + z_i, \quad (1b)$$

$$z_i = \max(x_i, 0), \quad (1c)$$

where x_i is the membrane potential or inner state of the neuron- i ; y_i is the variable of adaptation or fatigue; z_i is the firing rate; s_i is the constant input stimulus into the neuron- i ; $a_{ij} \geq 0$ is the synaptic weight from neuron- j to the neuron- i ; $b > 0$ is the constant determining adaptation intensity; $\tau_x > 0$ and $\tau_y > 0$ are the time constants of x_i and y_i , respectively. Here, a_{ij} is non-negative because the model supposes mutual inhibitions between neurons. No excitatory synapses or self-inhibitions are considered in this original form of the Matsuoka oscillator model. Although not specified in this study, the second is assumed as the time unit in most previous studies.

The outline of this model resembles regular recurrent neural networks (RNNs), adding the specific property of adaptation. The nonlinear transformation (1c) is the same as that of the rectified linear unit (ReLU) function, which is piecewise linear as follows:

$$z_i = \begin{cases} x_i & (x_i > 0) \\ 0 & (x_i \leq 0) \end{cases}. \quad (2)$$

Note that this activation function should have a firing threshold θ as $z_i = \max(x_i - \theta, 0)$. This threshold parameter can be, however, erased without loss of generality by redefining $x_i - \theta$ and $s_i - \theta$ as x_i and s_i , respectively.⁶ By applying this procedure, the threshold parameter θ can be ignored in this study.

Despite being named an ‘‘oscillator,’’ a single neuron in the Matsuoka oscillator model ($n = 1$) cannot sustainably oscillate by itself. According to the case classification (2), a single neuron follows different dynamics depending on the positivity or negativity of x_i . For $x_i \leq 0$, the system

(1) is rewritten as

$$\frac{d}{dt} \begin{bmatrix} x_i \\ y_i \end{bmatrix} = \begin{bmatrix} -\frac{1}{\tau_x} & -\frac{b}{\tau_x} \\ 0 & -\frac{1}{\tau_y} \end{bmatrix} \begin{bmatrix} x_i \\ y_i \end{bmatrix} + \begin{bmatrix} \frac{s_i}{\tau_x} \\ 0 \end{bmatrix}. \quad (3a)$$

Similarly, in the case $x_i > 0$,

$$\frac{d}{dt} \begin{bmatrix} x_i \\ y_i \end{bmatrix} = \begin{bmatrix} -\frac{1}{\tau_x} & -\frac{b}{\tau_x} \\ \frac{1}{\tau_y} & -\frac{1}{\tau_y} \end{bmatrix} \begin{bmatrix} x_i \\ y_i \end{bmatrix} + \begin{bmatrix} \frac{s_i}{\tau_x} \\ 0 \end{bmatrix}. \quad (3b)$$

In both cases, the single-neuron state $\begin{bmatrix} x_i & y_i \end{bmatrix}^\top$ asymptotically converges to stable fixed points. For $x_i > 0$, based on experimental knowledge, Ref. 6 introduced biological restriction for non-damped oscillation in the neuronal activities as follows:

$$\frac{(\tau_y - \tau_x)^2}{4\tau_x\tau_y} \geq b, \quad (4)$$

The adaptation process requires $\tau_y > \tau_x$, meaning that y_i is a slower variable than x_i . Additionally, Ineq. (4) requires even sufficient separation in the timescale between τ_y and τ_x . No oscillatory solution is possible in the case $n = 1$ of the Matsuoka oscillator model under these conditions for any input stimulus s_i , as shown in Fig. 1 in Ref. 6.

When mutually connected with inhibitory synapses, however, neurons of the Matsuoka oscillator model assume oscillatory properties as a network. In cases where more than three neurons are connected to each other ($n \geq 3$), many network topologies and corresponding diverse oscillation patterns can be observed as in Figs. 3–5 of Ref. 6. The following sections report on the case of $n = 2$ because the two-neuron model is the fundamental and simplest element of oscillatory circuits. This four-dimension system is written as

$$\tau_x \frac{dx_1}{dt} = -x_1 - by_1 - a_{12}z_2 + s_1, \quad (5a)$$

$$\tau_y \frac{dy_1}{dt} = -y_1 + z_1, \quad (5b)$$

$$\tau_x \frac{dx_2}{dt} = -x_2 - by_2 - a_{21}z_1 + rs_1, \quad (5c)$$

$$\tau_y \frac{dy_2}{dt} = -y_2 + z_2, \quad (5d)$$

$$z_1 = \max(x_1, 0), \quad (5e)$$

$$z_2 = \max(x_2, 0). \quad (5f)$$

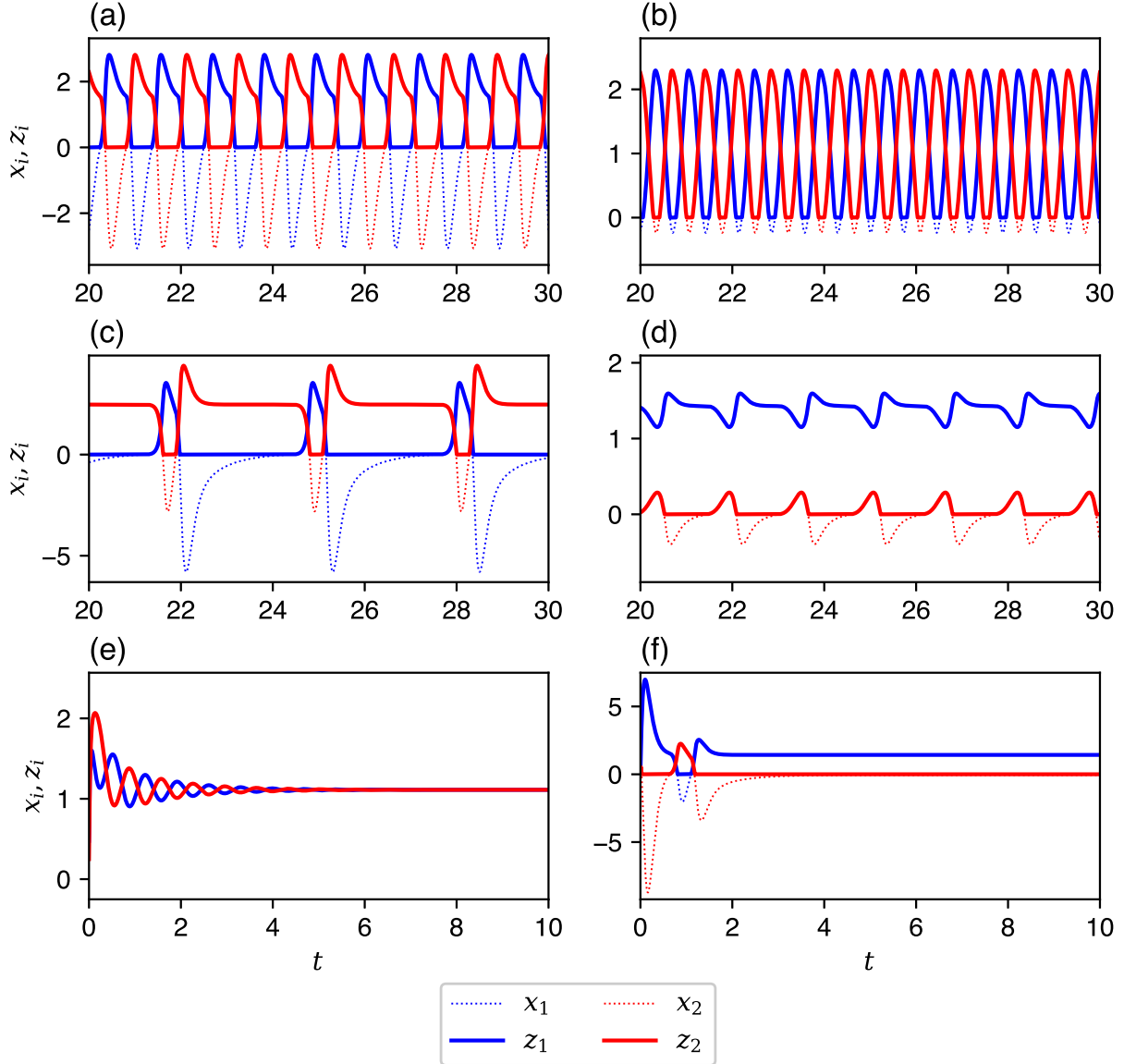


Fig. 1. Neuronal activity patterns for $n = 2$ of the Matsuoka oscillator model. Note that $a = a_{12} = a_{21}$, $r = \frac{s_2}{s_1}$, and the parameters b , τ_x , τ_y , and s_1 are all fixed as written in Subsection III A. (a) $a = 2$, $r = 1$. (b) $a = 2$, $r = 1.73$. (c) $a = 1.13$, $r = 1$. (d) $a = 1.6$, $r = 0.47$. (e) $a = 1$, $r = 1$. (f) $a = 2$, $r = 0.56$.

Here, we define a new parameter r as the input ratio between the two input stimuli

$$r := \frac{s_2}{s_1}. \quad (6)$$

Figure 1 shows several neuronal activity patterns as solutions of the two-neuron model (5) with symmetric connection $a = a_{12} = a_{21}$ and various values of r and a . Although the system does not

always have such oscillatory properties [e.g. Fig. 1(e), (f)], the observed oscillatory solutions are empirically stable limit cycles when it has them [e.g. Fig. 1(a)–(d)].

B. Existence Condition of Oscillatory Solutions

The original papers (Ref. 6 and 7) derived the condition for the existence of oscillatory solutions concerning synaptic connection a_{12} , a_{21} , and input ratio r . When $n = 2$, this condition is

$$\sqrt{a_{12}a_{21}} > a_{\text{inf}}, \quad (7a)$$

$$r > r_{\text{inf}}, \quad (7b)$$

$$r < r_{\text{sup}}, \quad (7c)$$

where

$$a_{\text{inf}} := 1 + \frac{\tau_x}{\tau_y}, \quad (8a)$$

$$r_{\text{inf}} := \frac{a_{21}}{1+b}, \quad (8b)$$

$$r_{\text{sup}} := \frac{1+b}{a_{12}}. \quad (8c)$$

Ineq. (7a) requires that synaptic weights a_{12} and a_{21} are sufficiently large. Ineqs. (7b) and (7c) provide a constraint for $r = \frac{s_2}{s_1}$ so that oscillatory solutions emerge when the level of input s_2 into the neuron-2 is roughly comparable with input s_1 into the neuron-1. From Ineqs. (7a)–(7c), a necessary condition for a_{12} and a_{21} is given as

$$1 + \frac{\tau_x}{\tau_y} < \sqrt{a_{12}a_{21}} < 1 + b. \quad (9)$$

Considering Ineqs. (4) and (9) together, we can obtain inequalities

$$\frac{\tau_x}{\tau_y} < b \leq \frac{(\tau_y - \tau_x)^2}{4\tau_x\tau_y}, \quad (10)$$

which forms an additional necessary condition for $\tau_x, \tau_y > 0$ as

$$\tau_y > 3\tau_x. \quad (11)$$

Precisely, e.g., the parameter setting in Ref. 8 does not satisfy Ineq. (11), which inappropriately results in permitting the damped oscillation of a single neuron.

Ineqs. (7a)–(7c) are the conditions under which there is no “stable” fixed point in the system. According to Ref. 6, any solutions of the general system (1a)–(1c) are proved to be bounded for $t \geq 0$. Hence, if Ineqs. (7a)–(7c) are satisfied, the system state does not converge to any fixed points but only travels in the bounded region; thus, nonstationary solutions occur. Note that these oscillations are empirically observed as limit cycles, which has not been mathematically guaranteed yet.

For the symmetric network $a = a_{12} = a_{21}$, we can rewrite Ineqs. (7a)–(7c) as

$$a > a_{\text{inf}}, \quad (12a)$$

$$r > r_{\text{inf}}, \quad (12b)$$

$$r < r_{\text{sup}}, \quad (12c)$$

where

$$a_{\text{inf}} := 1 + \frac{\tau_x}{\tau_y}, \quad (13a)$$

$$r_{\text{inf}} := \frac{a}{1+b}, \quad (13b)$$

$$r_{\text{sup}} := \frac{1+b}{a}. \quad (13c)$$

III. NUMERICAL OBSERVATIONS

A. Classification of Oscillation Types

Because we are interested in the effect of the neuronal interactions and external inputs, we do not consider the changes in values of b , τ_x , τ_y . Moreover, the multiplication of s_1 and s_2 by a common positive constant μ only increases the amplitude μ times with no change in the period or frequency of oscillation owing to the piecewise linearity of the system.⁷ Although s_1 is fixed, changing input ratio $r = \frac{s_2}{s_1}$ introduces an asymmetry between the external inputs into two neurons, which qualitatively transforms the system dynamics. Therefore, in the following discussions on the bifurcations of this model, we mainly attempt to vary parameters r , a_{12} , and a_{21} for fixed τ_x , τ_y , b , and s_1 values. Additionally, in all numerical simulations and figures in this study, we fix

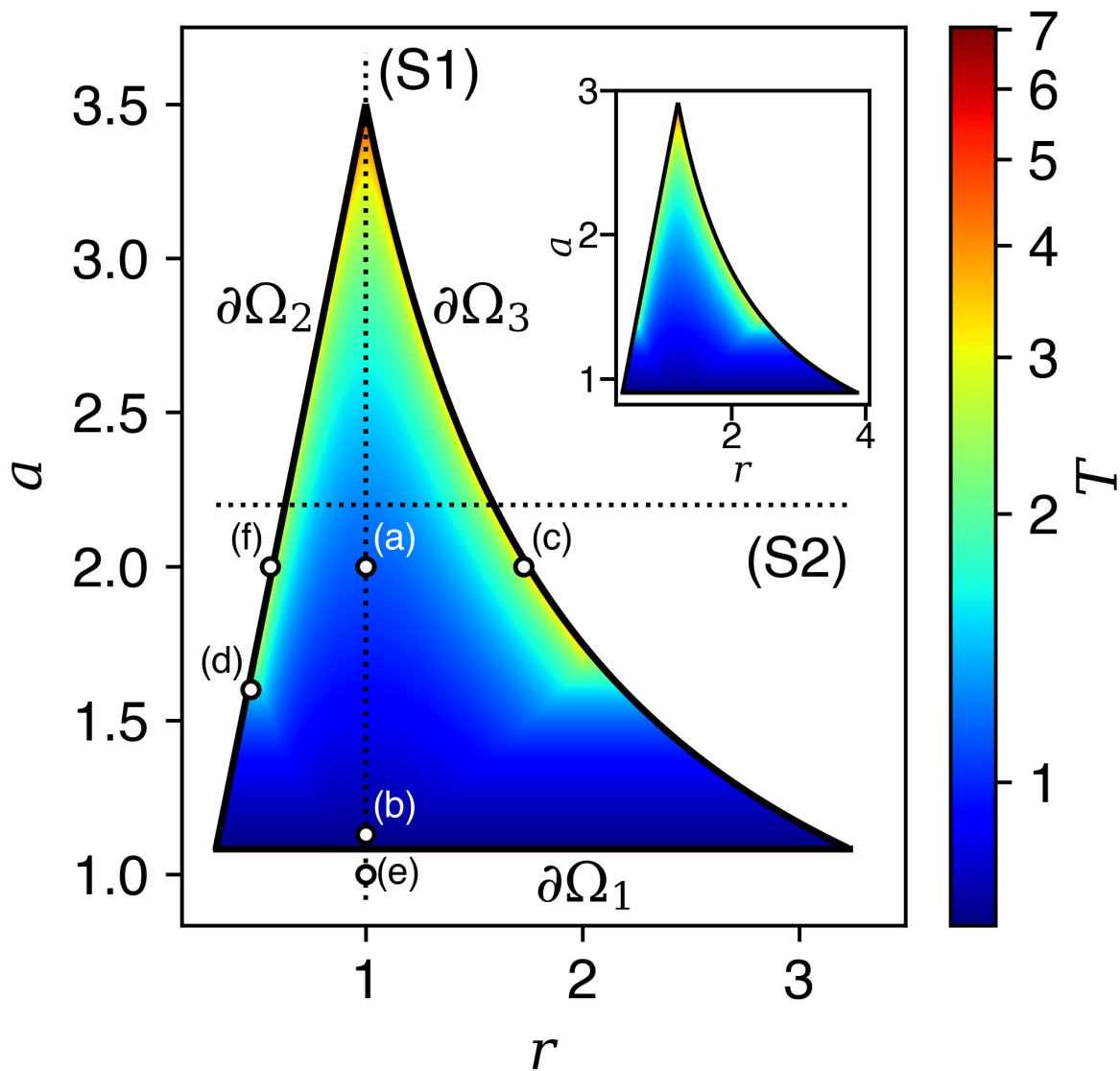


Fig. 2. Plot of oscillation period T of limit cycle solutions on the r - a plane in the symmetric case $a = a_{12} = a_{21}$ of the system (5). Oscillatory solutions exist only in Ω (T is plotted), which is surrounded by the three borderlines $\partial\Omega_1$, $\partial\Omega_2$, and $\partial\Omega_3$ (black solid lines). Each circle plot indicates the parameter set (r, a) corresponding to the activity patterns of Fig. 1(a)–(f). (Inset) the similar plot in the asymmetric connection case where $a = a_{12}$ and $a_{21} = 1.44a$.

$\tau_x = 0.05$, $\tau_y = 0.6$, $b = 2.5$, and $s_1 = 5$. Note that the positivity or negativity of s_1 is still important concerning the condition of existence for several fixed points, as discussed in the next section.

Figure 2 shows the oscillation period in the (r, a) space for the symmetric network $a = a_{12} =$

a_{21} . On this plane, three critical borderlines are defined by

$$\partial\Omega_1 := \{(r, a) \in \mathbb{R} \times \mathbb{R}_{>0} \mid a = a_{\text{inf}}\}, \quad (14a)$$

$$\partial\Omega_2 := \{(r, a) \in \mathbb{R} \times \mathbb{R}_{>0} \mid r = r_{\text{inf}}\}, \quad (14b)$$

$$\partial\Omega_3 := \{(r, a) \in \mathbb{R} \times \mathbb{R}_{>0} \mid r = r_{\text{sup}}\}, \quad (14c)$$

where a_{inf} , r_{inf} , and r_{sup} are given by Eqs. (13a)–(13c), respectively. Specifically, we can obtain a certain borderline threshold a_+^* , which meets $a_{\text{inf}} < a_+^* < 1 + b$, and can define the upper and lower parts of $\partial\Omega_2$ and $\partial\Omega_3$:

$$\partial\Omega_2^+ := \{(r, a) \in \mathbb{R} \times \mathbb{R}_{>0} \mid r = r_{\text{inf}}, a \geq a_+^*\}, \quad (15a)$$

$$\partial\Omega_2^- := \{(r, a) \in \mathbb{R} \times \mathbb{R}_{>0} \mid r = r_{\text{inf}}, a < a_+^*\}, \quad (15b)$$

$$\partial\Omega_3^+ := \{(r, a) \in \mathbb{R} \times \mathbb{R}_{>0} \mid r = r_{\text{sup}}, a \geq a_+^*\}, \quad (15c)$$

$$\partial\Omega_3^- := \{(r, a) \in \mathbb{R} \times \mathbb{R}_{>0} \mid r = r_{\text{sup}}, a < a_+^*\}. \quad (15d)$$

The borderlines $\partial\Omega_1$, $\partial\Omega_2$, and $\partial\Omega_3$ surround an area Ω , where Ineqs. (12a)–(12c) are all satisfied and stable limit cycles emerge:

$$\Omega := \{(r, a) \in \mathbb{R} \times \mathbb{R}_{>0} \mid a > a_{\text{inf}}, r_{\text{inf}} < r < r_{\text{sup}}\}. \quad (16)$$

In Ω , four qualitatively different types of oscillation patterns appear, as shown in Fig. 1(a)–(d);

- Oscillation type (a) shown in Fig. 1(a)
Of those discussed in previous studies, the most typical is this, where the neurons alternate between the firing and resting modes.
- Oscillation type (b) shown in Fig. 1(b)
This is a relatively small and fast oscillation in the vicinity of $\partial\Omega_1$, where the oscillation period is virtually independent from r and decreases as a decreases.
- Oscillation type (c) shown in Fig. 1(c)
This emerges near $\partial\Omega_2^+$ and $\partial\Omega_3^+$ when a is greater than or equal to a_+^* . In the neighborhoods of these borderlines, a neurons firing duration is greatly extended. On the borderline $\partial\Omega_2^+$ or $\partial\Omega_3^+$, this neuron fires constantly while the other neuron remains quiescent, as shown in Fig. 1(f).

- Oscillation type (d) shown in Fig. 1(d)

This is the remaining non-trivial oscillation type observed when $a < a_+^*$ and r are near borderlines $\partial\Omega_2^-$ and $\partial\Omega_3^-$. This pattern has an invariant oscillation period under a fixed value of a . In this pattern, only one neuron is permanently excited while the other alternates between the firing and quiescent states.

As discussed later, there are additional borderlines Δ_1 and Δ_2 between the oscillation pattern (d) and the other patterns (a)–(c) on the (r, a) space (see Fig. 5). The borderline threshold value a_+^* above is derived in Subsection V B. Note that the three critical borderlines $\partial\Omega_1$, $\partial\Omega_2$ and $\partial\Omega_3$ defined by Eqs. (14a)–(14c) can be also generalized to the asymmetric connection case $a_{12} \neq a_{21}$, where the values of a_{inf} , r_{inf} , and r_{sup} are in the asymmetric version given by Eqs. (8a)–(8c), respectively (displayed on the inset of Fig. 2).

B. Approximation of Oscillation Period

Ref. 8 provided an approximated angular frequency of the limit cycle oscillation ω in the symmetric case $a = a_{12} = a_{21}$ and $r = \frac{s_2}{s_1} = 1$:

$$\omega = \frac{1}{\tau_y} \sqrt{\frac{(\tau_x + \tau_y)b - \tau_x a}{\tau_x a}}. \quad (17)$$

Using this expression, we obtain the approximated oscillation period, T_{harm} , as

$$T_{\text{harm}} := \frac{2\pi}{\omega} = 2\pi\tau_y \sqrt{\frac{\tau_x a}{(\tau_x + \tau_y)b - \tau_x a}}. \quad (18)$$

Eq. (17) is based on the approximations of x_i by a pure sinusoidal wave and the system (5) by a harmonic oscillator. This is a good approximation when the nonlinear transformation from x_i to z_i given by Eq. (2) does not change the overall waveform (i.e., $x_i \geq 0$ at almost all timepoints). This corresponds to a critical behavior as the oscillation type (b) seen in the vicinity of $\partial\Omega_1$. Figure. 3 plots the actual oscillation periods (circle) and the approximated oscillation periods given by Eq. (18) (dotted line) along the cross-section (S1) are represented by the vertical dotted line in Fig. 2. As the value of a decreases to a_{inf} , the theoretical prediction T_{harm} approaches the numerically observed oscillation period T .

Two main problems arise concerning the approximation form T_{harm} given by Eq. (18). First, T_{harm} is less accurate when a is sufficiently large to approach borderlines $\partial\Omega_2$ and $\partial\Omega_3$. This

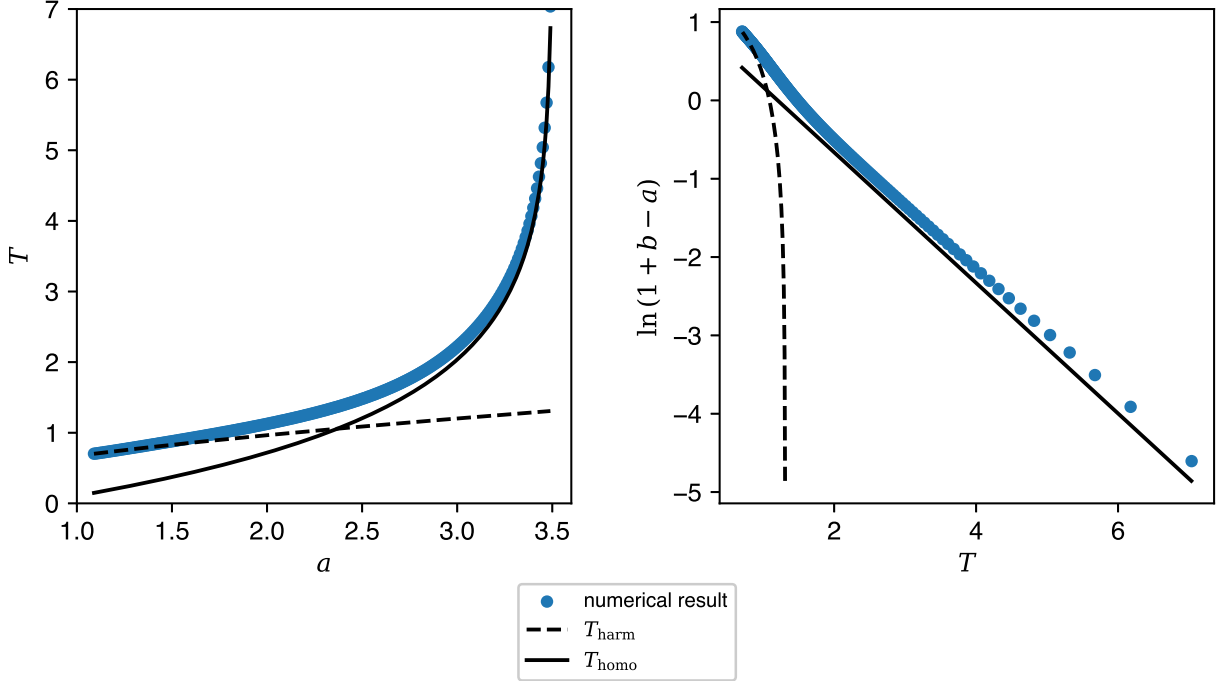


Fig. 3. (Left) Plot of the oscillation period T vs the symmetric synaptic weight a with a fixed value $r = 1$ corresponding to the dotted line (S1) in Fig. (2). (Right) Another plot version of $\ln(1 + b - a)$ vs the oscillation period T .

is because the larger the waveform distortion from x_i to z_i , the poorer the prediction accuracy of Eq. (17), as mentioned in Ref. 8. Second, T_{harm} can be only applied to the case $a = a_{12} = a_{21}$ and $r = 1$, which corresponds to the line (S1) in Fig. 2. This means that asymmetric oscillations like the oscillation type (c) cannot be well evaluated by the approximation form T_{harm} .

Numerical observations imply the logarithmic divergence of the oscillation period under the larger value of a . In Subsection VC, we propose a novel scaling law given by T_{homo} , which can roughly approximate this logarithmic divergence [as represented by solid lines in Fig. 3]. We see that this approximation T_{homo} is also applicable to the cases of $a_{12} \neq a_{21}$ and $r \neq 1$, unlike the previous approximation T_{harm} .

IV. EXISTENCE AND STABILITY OF FIXED POINTS

Within a single linear dynamical system, only a neutrally stable oscillation around a center is possible and no stable limit cycle emerges as a periodic solution. Nevertheless, a typical class of hybrid systems, the piecewise affine system, which consists of several discretely combined linear

systems, sometimes possesses nontrivial solutions of stable limit cycles. The Matsuoka oscillator model is an example of the piecewise affine systems, as shown in Section IV, because the system dynamics switch discontinuously across the x_1 -axis and x_2 -axis that represent the boundaries $x_i = 0$ of Eq. (2).

Now, we apply fixed point analyses to the $n = 2$ model (5) for a precise discussion regarding the existence and stability of fixed points, which corresponds to stationary neuronal activities observed in Fig. 1(e), (f). As we see later, these analyses are essential for understanding the generation and bifurcation mechanism of limit cycle oscillations and deriving the oscillation period prediction (34). For convenience, we represent a system state or a phase point \mathbf{X} in the phase space \mathbb{R}^4 :

$$\mathbf{X} := \begin{bmatrix} x_1 & y_1 & x_2 & y_2 \end{bmatrix}^\top. \quad (19)$$

We also define an operator $[\cdot]_q$ that extracts the q -coordinate of the variable (e.g. $[\mathbf{X}]_{y_1} = y_1$).

Depending on the positivity or non-positivity of x_1 and x_2 , we can divide the phase space \mathbb{R}^4 into four different regions, which correspond to four orthants on the x_1 - x_2 plane

$$\begin{aligned} S_A &:= \{ \mathbf{X} \in \mathbb{R}^4 \mid x_1, x_2 \leq 0 \}, \\ S_B &:= \{ \mathbf{X} \in \mathbb{R}^4 \mid x_1 > 0, x_2 \leq 0 \}, \\ S_C &:= \{ \mathbf{X} \in \mathbb{R}^4 \mid x_1 \leq 0, x_2 > 0 \}, \\ S_D &:= \{ \mathbf{X} \in \mathbb{R}^4 \mid x_1, x_2 > 0 \}. \end{aligned} \quad (20)$$

These regions are divided by the discontinuity boundaries below, which are defined as three-dimensional manifolds corresponding to parts of the x_1 - and x_2 -axes

$$\begin{aligned} \Sigma_{AB} = \Sigma_{BA} &:= \{ \mathbf{X} \in \mathbb{R}^4 \mid x_1 = 0, x_2 \leq 0 \}, \\ \Sigma_{BD} = \Sigma_{DB} &:= \{ \mathbf{X} \in \mathbb{R}^4 \mid x_1 > 0, x_2 = 0 \}, \\ \Sigma_{AC} = \Sigma_{CA} &:= \{ \mathbf{X} \in \mathbb{R}^4 \mid x_1 \leq 0, x_2 = 0 \}, \\ \Sigma_{CD} = \Sigma_{DC} &:= \{ \mathbf{X} \in \mathbb{R}^4 \mid x_1 = 0, x_2 > 0 \}, \end{aligned} \quad (21)$$

Note that through this paper, unless there is any confusion, the discontinuity boundaries in the phase space above are all termed as ‘‘boundaries,’’ which are distinguished from ‘‘borderlines’’ such as $\partial\Omega_1$ and Δ_1 in the (r, a) parameter space. Although notation couples such as Σ_{CD} and Σ_{DC} refer to the same switching manifold, in this study, they are labeled separately depending on which direction the system state follows through this manifold. For example, when the system state transits from S_C into S_D , it is designated as crossing Σ_{CD} ; when it goes from S_D into S_C , it is represented as crossing Σ_{DC} .

Similar to the single neuron analysis (Subsection II A), the two-neuron system (5) can be represented as a set of four linear systems by replacing z_i with either x_i or 0 according to Eq. (2). The linear dynamics of each is defined within one of the divided regions. For instance, within region S_i ($i \in \{A, B, C, D\}$), the dynamic is

$$\frac{d\mathbf{X}}{dt} = J_i \mathbf{X} + \mathbf{s}, \quad (22)$$

where $\mathbf{s} = \left[\frac{s_1}{\tau_x} \ 0 \ \frac{s_2}{\tau_x} \ 0 \right]^\top$. A fixed point \mathbf{X}_i^* of these dynamics meet $\frac{d\mathbf{X}}{dt} = \mathbf{0}$, or

$$J_i \mathbf{X}_i^* + \mathbf{s} = \mathbf{0}, \quad (23)$$

the stability of which is characterized by the eigenvalues of matrix J_i ; if at least one of the eigenvalues λ_i has a positive real part, the fixed point \mathbf{X}_i^* is unstable because the trajectories of the system repelled from it in the corresponding eigendirection. Conversely, when the real parts of all eigenvalues are negative, the fixed point is stable.¹⁷ In this sense, J_i is equivalent to the Jacobian matrix around the fixed point \mathbf{X}_i^* . Note that the stability here means linear and asymptotic stability.

A key point is that the fixed point \mathbf{X}_i^* is determined corresponding to the dynamics $\frac{d\mathbf{X}}{dt} = J_i \mathbf{X} + \mathbf{s}$, independently of the region S_i . This means that $\mathbf{X}_i^* \in S_i$ is not always true. Suppose that

$$\mathbf{X}_i^* \in S_j \ (j \neq i), \quad (24)$$

then \mathbf{X}_i^* does not exist, or in other words, is a “virtual” fixed point¹⁸ because the system state at \mathbf{X}_i^* can follow

$$\frac{d\mathbf{X}}{dt} = J_j \mathbf{X}_i^* + \mathbf{s} \neq \mathbf{0}, \quad (25)$$

so that the system is no longer stationary in this situation (see also Fig. 4). Conversely, if

$$\mathbf{X}_i^* \in S_i, \quad (26)$$

then the fixed point \mathbf{X}_i^* is regarded as “regular” (or “admissible”) because it exists.^{18,19} Differently expressed, the condition (26) provides the existence condition of \mathbf{X}_i^* . In the following subsections, the four cases of dynamics are investigated for each index $i \in \{A, B, C, D\}$, regarding

- the Jacobian matrix J_i ,
- the fixed point \mathbf{X}_i^* ,

- the eigenvalues λ_i , and
- the existence condition $\mathbf{X}_i^* \in S_i$.

A. Dynamics in the Region S_A

$$J_A = \begin{bmatrix} -\frac{1}{\tau_x} & -\frac{b}{\tau_x} & 0 & 0 \\ 0 & -\frac{1}{\tau_y} & 0 & 0 \\ 0 & 0 & -\frac{1}{\tau_x} & -\frac{b}{\tau_x} \\ 0 & 0 & 0 & -\frac{1}{\tau_y} \end{bmatrix}, \quad (27a)$$

$$\mathbf{X}_A^* = \begin{bmatrix} s_1 & 0 & rs_1 & 0 \end{bmatrix}^\top, \quad (27b)$$

$$\lambda_A = -\frac{1}{\tau_x}, -\frac{1}{\tau_y}. \quad (27c)$$

This case is the simplest because neither neuron fires, resulting in no reciprocal interaction between the two. In this sense, each neuron can be treated as an independent single neuron. The existence condition $\mathbf{X}_A^* \in S_A$ is

$$s_1, rs_1 \leq 0. \quad (27d)$$

It is obvious that \mathbf{X}_A^* is stable because the eigenvalues (27c) are negative real numbers.

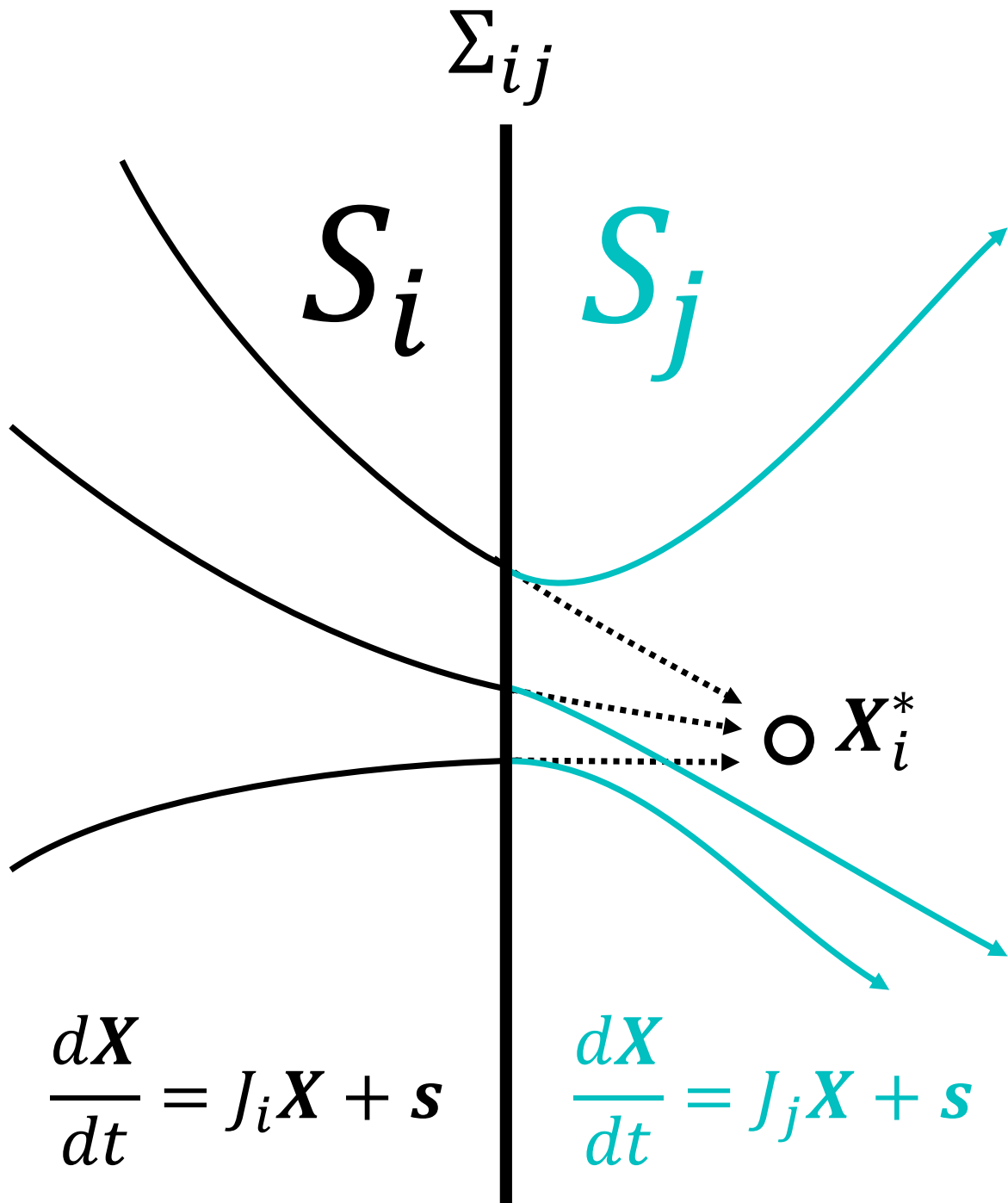


Fig. 4. Conceptual example of a virtual fixed point. Suppose that a fixed point \mathbf{X}_i^* determined with respect to dynamics $\frac{d\mathbf{X}}{dt} = J_i \mathbf{X} + \mathbf{s}$ is stable but virtual because $\mathbf{X}_i^* \in S_j$; when the system state is in the region S_i , it is about to converge to \mathbf{X}_i^* ; after crossing the boundary Σ_{ij} , however, the system state comes to follow the other dynamics $\frac{d\mathbf{X}}{dt} = J_j \mathbf{X} + \mathbf{s}$; thus, \mathbf{X}_i^* no longer functions as a stable fixed point in S_j .

B. Dynamics in the Region S_B

$$J_B = \begin{bmatrix} -\frac{1}{\tau_x} & -\frac{b}{\tau_x} & 0 & 0 \\ \frac{1}{\tau_y} & -\frac{1}{\tau_y} & 0 & 0 \\ -\frac{a_{21}}{\tau_x} & 0 & -\frac{1}{\tau_x} & -\frac{b}{\tau_x} \\ 0 & 0 & 0 & -\frac{1}{\tau_y} \end{bmatrix}, \quad (28a)$$

$$\mathbf{X}_B^* = \left[\frac{s_1}{1+b} \quad \frac{s_1}{1+b} \quad \frac{(1+b)r - a_{21}}{1+b} s_1 \quad 0 \right]^\top, \quad (28b)$$

$$\lambda_B = -\frac{1}{\tau_x}, -\frac{1}{\tau_y}, \frac{-\tau_x - \tau_y \pm \sqrt{Q_B}}{2\tau_x\tau_y}, \quad (28c)$$

where $Q_B = (\tau_y - \tau_x)^2 - 4b\tau_x\tau_y$. The existence condition $\mathbf{X}_B^* \in S_B$ is

$$s_1 > 0 \quad \text{and} \quad r \leq \frac{a_{21}}{1+b}. \quad (28d)$$

In this case, neuron-2 is significantly more strongly inhibited by neuron-1 than the direct external input s_2 ; therefore, with only the neuron-1 activated, the neuron-2 no longer fires. Two of the eigenvalues $\lambda_B = -\frac{1}{\tau_x}, -\frac{1}{\tau_y}$ are both negative real numbers, and the same holds for the remaining two $\lambda_B = \frac{-\tau_x - \tau_y \pm \sqrt{Q_B}}{2\tau_x\tau_y}$ because of the non-damped oscillation condition (4). Therefore, \mathbf{X}_B^* is a stable node. The neuronal activity pattern shown in Fig. 1(f) corresponds to the convergence to \mathbf{X}_B^* .

C. Dynamics in the Region S_C

$$J_C = \begin{bmatrix} -\frac{1}{\tau_x} & -\frac{b}{\tau_x} & -\frac{a_{12}}{\tau_x} & 0 \\ 0 & -\frac{1}{\tau_y} & 0 & 0 \\ 0 & 0 & -\frac{1}{\tau_x} & -\frac{b}{\tau_x} \\ 0 & 0 & \frac{1}{\tau_y} & -\frac{1}{\tau_y} \end{bmatrix}, \quad (29a)$$

$$\mathbf{X}_C^* = \left[\frac{(1+b)-ra_{12}}{1+b}s_1 \quad 0 \quad \frac{rs_1}{1+b} \quad \frac{rs_1}{1+b} \right]^\top, \quad (29b)$$

$$\lambda_C = -\frac{1}{\tau_x}, -\frac{1}{\tau_y}, \frac{-\tau_x - \tau_y \pm \sqrt{Q_C}}{2\tau_x\tau_y}, \quad (29c)$$

where $Q_C = (\tau_y - \tau_x)^2 - 4b\tau_x\tau_y$. This case is completely symmetric to the dynamics in the region S_B , with indices 1 and 2 switching to each other. The existence condition of $\mathbf{X}_C^* \in S_C$ is

$$s_2 = rs_1 > 0 \quad \text{and} \quad \frac{1}{r} \leq \frac{a_{12}}{1+b}. \quad (29d)$$

D. Dynamics in the Region S_D

$$J_D = \begin{bmatrix} -\frac{1}{\tau_x} & -\frac{b}{\tau_x} & -\frac{a_{12}}{\tau_x} & 0 \\ \frac{1}{\tau_y} & -\frac{1}{\tau_y} & 0 & 0 \\ -\frac{a_{21}}{\tau_x} & 0 & -\frac{1}{\tau_x} & -\frac{b}{\tau_x} \\ 0 & 0 & \frac{1}{\tau_y} & -\frac{1}{\tau_y} \end{bmatrix}. \quad (30a)$$

This is the most complicated case and requires a fixed-point analysis of \mathbf{X}_D^* . If $(1+b)^2 \neq$

$a_{12}a_{21}$, then \mathbf{X}_D^* is written as

$$\mathbf{X}_D^* = \frac{s_1}{(1+b)^2 - a_{12}a_{21}} \begin{bmatrix} (1+b) - ra_{12} \\ (1+b) - ra_{12} \\ (1+b)r - a_{21} \\ (1+b)r - a_{21} \end{bmatrix}. \quad (30b)$$

In the remaining singular case $1+b = \sqrt{a_{12}a_{21}}$, the fixed point cannot be simply written as Eq. (30b). If $(ra_{12} - \sqrt{a_{12}a_{21}})s_1 = 0$ in addition to $1+b = \sqrt{a_{12}a_{21}}$, a set of non-isolated fixed points is represented as a line in the four-dimensional system space:

$$\mathbf{X}_D^* = \left\{ \mathbf{X} \in \mathbb{R}^4 \mid x_2 = -\sqrt{\frac{a_{21}}{a_{12}}}x_1 + \frac{1}{a_{12}}s_1, y_1 = x_1, y_2 = x_2 \right\}. \quad (30c)$$

Note that \mathbf{X}_B^* and \mathbf{X}_C^* are both on the line (30g) in these conditions. By contrast, no solution satisfies $\frac{d\mathbf{X}}{dt} = 0$ when $(ra_{12} - \sqrt{a_{12}a_{21}})s_1 \neq 0$.

Whether or not the fixed point \mathbf{X}_D^* is written as Eq. (30b) or (30g), its stability is determined by the eigenvalues λ_D , which are solutions of the characteristic equation $\det(\lambda_D I - J_D) = 0$. Here,

$$\begin{aligned} & \det(\lambda_D I - J_D) \\ &= \left(\lambda_D^2 + \frac{\tau_x + \tau_y + \tau_y \sqrt{a_{12}a_{21}}}{\tau_x \tau_y} \lambda_D + \frac{1+b + \sqrt{a_{12}a_{21}}}{\tau_x \tau_y} \right) \\ & \times \left(\lambda_D^2 + \frac{\tau_x + \tau_y - \tau_y \sqrt{a_{12}a_{21}}}{\tau_x \tau_y} \lambda_D + \frac{1+b - \sqrt{a_{12}a_{21}}}{\tau_x \tau_y} \right). \end{aligned} \quad (30d)$$

The real parts of the first two eigenvalues represented by λ_{D+} as the solutions of

$$\lambda_{D+}^2 + \frac{\tau_x + \tau_y + \tau_y \sqrt{a_{12}a_{21}}}{\tau_x \tau_y} \lambda_{D+} + \frac{1+b + \sqrt{a_{12}a_{21}}}{\tau_x \tau_y} = 0, \quad (30e)$$

are always negative, which suggests that the dynamics converge to \mathbf{X}_D^* on the plane spanned by the two corresponding eigenvectors \mathbf{v}_{D+} .

The remaining two eigenvalues λ_{D-} are given by the equation

$$\lambda_{D-}^2 + \frac{\tau_x + \tau_y - \tau_y \sqrt{a_{12}a_{21}}}{\tau_x \tau_y} \lambda_{D-} + \frac{1+b - \sqrt{a_{12}a_{21}}}{\tau_x \tau_y} = 0. \quad (30f)$$

The two corresponding eigenvectors \mathbf{v}_{D-} span a plane on the phase space

$$P_D := \left\{ \mathbf{X} \in \mathbb{R}^4 \mid x_2 = -\sqrt{\frac{a_{21}}{a_{12}}}x_1 + \frac{r + \sqrt{\frac{a_{21}}{a_{12}}}}{1+b + \sqrt{a_{12}a_{21}}}s_1, y_2 = -\sqrt{\frac{a_{21}}{a_{12}}}y_1 + \frac{r + \sqrt{\frac{a_{21}}{a_{12}}}}{1+b + \sqrt{a_{12}a_{21}}}s_1 \right\}. \quad (30g)$$

According to the discussion above, the system state outside P_D is asymptotically attracted to P_D through the stable eigendirections v_{D+} . This means that the stability of \mathbf{X}_D^* is finally determined as the stability on the two-dimensional plane P_D , according to the values of λ_{D-} ,¹⁷

- \mathbf{X}_D^* is a stable node or spiral if

$$\sqrt{a_{12}a_{21}} < \min\left(1 + \frac{\tau_x}{\tau_y}, 1 + b\right). \quad (30h)$$

Figure. 1(e) is the neuronal activity converging to \mathbf{X}_D^* , where \mathbf{X}_D^* is a regular stable spiral.

- \mathbf{X}_D^* becomes a center if

$$\sqrt{a_{12}a_{21}} = 1 + \frac{\tau_x}{\tau_y} < 1 + b. \quad (30i)$$

Conservative oscillation occurs around it on the plane spanned by the two corresponding eigenvectors.

- \mathbf{X}_D^* behaves as an unstable node or spiral, if

$$1 + \frac{\tau_x}{\tau_y} < \sqrt{a_{12}a_{21}} < 1 + b, \quad (30j)$$

which repels from the remaining two eigendirections if

- \mathbf{X}_D^* comprises non-isolated fixed points written as Eq. (30g), if

$$\sqrt{a_{12}a_{21}} = 1 + b, \quad (30k)$$

where one eigenvalue, λ_{D-} , is 0 and the corresponding eigenvector is parallel to the line (30g). This is equivalent to the non-isolated fixed point as the line given by Eq. (30g). Additionally, in the remaining eigendirection, \mathbf{X}_D^* attracts if $b < \frac{\tau_x}{\tau_y}$, and repels if $\frac{\tau_x}{\tau_y} < b$. If $\sqrt{a_{12}a_{21}} = 1 + b = 1 + \frac{\tau_x}{\tau_y}$, then \mathbf{X}_D^* becomes further non-isolated fixed points as a plane equal to P_D .

- \mathbf{X}_D^* is a saddle point if

$$1 + b < \sqrt{a_{12}a_{21}}. \quad (30l)$$

Trajectories are repelled from \mathbf{X}_D^* in a single eigendirection corresponding to a positive eigenvalue λ_{D-} .

The existence condition $\mathbf{X}_D^* \in S_D$ is also separately discussed depending on the relation between $1 + b$ and $\sqrt{a_{12}a_{21}}$.

- When $1 + b > \sqrt{a_{12}a_{21}}$, $\mathbf{X}_D^* \in S_D$ is true if and only if

$$\frac{1+b}{a_{12}} > r > \frac{a_{21}}{1+b} > 0 \quad \text{and} \quad s_1 > 0. \quad (30m)$$

In this situation, the necessary and sufficient condition below is also true.

$$\mathbf{X}_A^* \notin A \text{ and } \mathbf{X}_B^* \notin B \text{ and } \mathbf{X}_C^* \notin C \iff \mathbf{X}_D^* \in S_D. \quad (30n)$$

- When $1 + b = \sqrt{a_{12}a_{21}}$, $\mathbf{X}_D^* \in S_D$ is true if and only if

$$r = \frac{1+b}{a_{12}} = \frac{a_{21}}{1+b} > 0 \quad \text{and} \quad s_1 > 0. \quad (30o)$$

Note that the repelling eigendirection of \mathbf{X}_D^* leads to \mathbf{X}_B^* or \mathbf{X}_C^* .

- When $1 + b < \sqrt{a_{12}a_{21}}$, $\mathbf{X}_D^* \in S_D$ is true if and only if

$$\frac{a_{21}}{1+b} > r > \frac{1+b}{a_{12}} > 0 \quad \text{and} \quad s_1 > 0. \quad (30p)$$

This agrees with the condition under which \mathbf{X}_D^* becomes a saddle point.

In all cases, a necessary condition for $\mathbf{X}_D^* \in S_D$ is described as

$$s_1, r > 0.$$

Consequently, the external inputs into the neuron-1 and neuron-2 are both excitatory.

V. BIFURCATIONS BETWEEN FIXED POINTS AND OSCILLATORY SOLUTIONS

According to Ineqs. (27d), the stable fixed point \mathbf{X}_A^* does not exist when the two neurons are both suppressed by non-positive inputs. The other three fixed points \mathbf{X}_B^* , \mathbf{X}_C^* , \mathbf{X}_D^* can exist when at least s_1 or $s_2 = rs_1$ is positive. Specifically,

- the existence conditions $\mathbf{X}_B^* \in S_B$ given by (28d),
- the existence conditions $\mathbf{X}_C^* \in S_C$ given by (28c), and
- the conditions (30h) and (30m) under which $\mathbf{X}_D^* \in S_D$ is a stable fixed point,

are all separated from the existence condition of the oscillatory solutions Ineqs. (7a)–(7c). Otherwise expressed, if any oscillation occurs under the conditions (7a)–(7c), then

$$\mathbf{X}_B^*, \mathbf{X}_C^*, \mathbf{X}_D^* \in S_D, \quad (31)$$

which means that only \mathbf{X}_D^* is regular while \mathbf{X}_B^* and \mathbf{X}_C^* are virtual fixed points. Satisfying Ineqs. (7a)–(7c) leads to the necessary condition (9), which is equivalent to Ineqs. (30j). Hence, the existing fixed point \mathbf{X}_D^* is an unstable node or spiral. Figure 5, which shows the same r - a plane as Fig. 2, is a phase diagram specifying the parameter regions where either \mathbf{X}_B^* , \mathbf{X}_C^* , \mathbf{X}_D^* , or oscillatory solutions of the types (a)–(d) exist as attractors. The overlapped purple area of Fig. 5 satisfies both (28d) and (29d); thus, stable fixed points \mathbf{X}_B^* and \mathbf{X}_C^* exist simultaneously.

A. Emergence Mechanism of Oscillatory Solutions

Figure 6 displays the same oscillation patterns (a)–(d) as in Fig. 1(a)–(d) on the x_1 - x_2 plane (left column) and in the x_1 - x_2 - Y space (right column) for $Y = y_1 - y_2$. Note that the latter plot format is effective for observing overviews of the oscillation trajectories as previously proposed in Ref. 8. Here, the emergence mechanism of oscillations under the conditions (7a)–(7c) is explained as repetitions of convergence to the stable but virtual \mathbf{X}_B^* , \mathbf{X}_C^* and divergence from the regular but unstable \mathbf{X}_D^* . Since (31), if the system state is currently in the region S_B (or S_C), it transits across the boundary Σ_{BD} (Σ_{CD}) into the region S_D before converging to \mathbf{X}_B^* (\mathbf{X}_C^*) [the cyan (magenta) dotted lines shown in Fig. 6 are the imaginary extended trajectories assumed if this convergence continues in the region S_D]. In the region S_D , the system state follows the dynamics $\frac{d\mathbf{X}}{dt} = J_D\mathbf{X} + \mathbf{s}$, in the eigendirection \mathbf{v}_{D+} gets attracted to the plane P_D , and in turn, escapes from S_D and crosses Σ_{DC} , Σ_{DB} , (Σ_{DB} , or Σ_{DC}). In the oscillation types (a)–(c), the system state transits across Σ_{DC} (Σ_{DB}) into S_C (S_B), after which the system state follows similar itineraries from S_C (S_B) to S_D and returns to S_B (S_C):

$$S_B \rightarrow S_D \rightarrow S_C \rightarrow S_D \rightarrow S_B \rightarrow S_D \rightarrow S_C \rightarrow \cdots .$$

The remaining oscillation type (d) is exceptional because the system state immediately returns to S_B (S_C) across Σ_{DB} (Σ_{DC}); thus, the periodic orbit is captured in regions S_D and S_B (S_C) like

$$S_B \rightarrow S_D \rightarrow S_B \rightarrow S_D \rightarrow S_B \rightarrow S_D \rightarrow S_B \rightarrow \cdots ,$$

Note that if the system state is currently in region S_A , it is immediately transferred into the regions S_B , S_C , or S_D similar to the convergence to the virtual stable fixed point \mathbf{X}_A^* outside S_A .

B. Bifurcation Scenarios

The oscillation types (b)–(d) represent those observed in the neighborhoods of the borderlines $\partial\Omega_1$, $\partial\Omega_2$, and $\partial\Omega_3$ in the parameter space of Fig. 5. Here, we can expect several bifurcation scenarios to emerge between these limit cycles and fixed points (Fig. 7). The first is a subcritical Hopf-like bifurcation observed on the borderline $\partial\Omega_1$, where the stability of \mathbf{X}_D^* changes from an unstable spiral via a center to a stable spiral [Fig. 7(I)]. The previously proposed approximation of the oscillation period (18) completely coincides in the actual oscillation period at the borderline $\partial\Omega_1$, which is identical to the harmonic oscillation period around the center \mathbf{X}_D^* . In this bifurcation point, the outermost periodic orbit grazing either or both S_B and S_C can be regarded as semihalf; it is neutrally stable from and toward its interior; and is attracting from its exterior because of the attracting flow in the outer regions S_B and S_C toward S_D . Beyond $\partial\Omega_1$ in the parameter space, the periodic orbits across multiple regions disappear because the system dynamics in the region S_D are now incapable of carrying the system state through divergence outward to S_B or S_C . Through this scenario, the limit cycle instantaneously emerges with non-zero (sufficiently large) value of oscillation amplitude, which is a canard-like behavior.

The second bifurcation is homoclinic-like, which emerges at $\partial\Omega_2^+$ and $\partial\Omega_3^+$. The oscillation type (c) is close to this bifurcation. In the vicinity of $\partial\Omega_2^+$ (or $\partial\Omega_3^+$), the virtual stable fixed point \mathbf{X}_B^* (\mathbf{X}_C^*) becomes regular upon entering the region S_B (S_C) on the pre-existing limit cycle orbit [Fig. 7(II)]. When the parameter set (r, a) is on the $\partial\Omega_2^+$ ($\partial\Omega_3^+$), then \mathbf{X}_B^* (\mathbf{X}_C^*) is precisely on the boundary Σ_{BD} (Σ_{CD}) and identical to \mathbf{X}_C^* , which is termed a boundary equilibrium.^{18,19} Because \mathbf{X}_B^* (\mathbf{X}_C^*) attracts from S_B (S_C) and repels into S_D , it functions as a saddle-like point [this behavior is reflected in Fig. 6(c)]. At this bifurcation point, the regularity of \mathbf{X}_D^* and the virtuality of \mathbf{X}_B^* can be regarded as exchanged with each other. This is termed a persistence, a type of boundary-equilibrium bifurcation.^{18,19} At the intersection of $\partial\Omega_2$ and $\partial\Omega_3$, where $(r, a) = (1, 1 + b)$, this homoclinic-like bifurcation becomes codimension-two through which two homoclinic orbits are expected to merge into a heteroclinic orbit.

Finally, the bifurcation pattern corresponding to the oscillation type (d) emerges on $\partial\Omega_2^-$ and $\partial\Omega_3^-$. Similar to the homoclinic-like bifurcation, \mathbf{X}_D^* disappears and \mathbf{X}_B^* (or \mathbf{X}_C^*) comes to exist through a persistence [Fig. 7(III)], when r or a crosses the borderline $\partial\Omega_2^-$ ($\partial\Omega_3^-$). However, in this bifurcation, the limit cycle trajectories as the combination of divergence from \mathbf{X}_D^* and convergence to \mathbf{X}_B^* (\mathbf{X}_C^*) become extremely small [see also Fig. 6(d)], converging to zero oscil-

lation amplitudes. Although the oscillation period is constant in the neighborhoods of the borderlines (mentioned in Section III A), this bifurcation seems supercritical Hopf-like, or a so-called discontinuity-induced Hopf bifurcation.¹⁹

The second homoclinic-like bifurcation and the third supercritical Hopf-like bifurcation are both boundary-equilibrium bifurcations caused by regular-virtual exchanges between fixed points, through which their stability or instability is conserved. Corresponding to the (c) and (d) oscillation pattern, these bifurcations are distinguished by whether \mathbf{X}_D^* works as an unstable node or an unstable spiral. If \mathbf{X}_D^* is an unstable node, then the dynamics in the region S_D certainly transport the system state from Σ_{BD} (or Σ_{CD}) to the opposite side Σ_{DC} (or Σ_{DB}), in the fastest eigendirection corresponding to one of λ_{D-} with the largest absolute value [the lower black solid line shown in the right of Fig. 6(c) is almost straight, which is extremely close to this eigendirection]. Conversely, when \mathbf{X}_D^* is an unstable spiral, the rotational dynamics around this point can afterward return the system state coming from Σ_{BD} (Σ_{CD}) to the same side Σ_{DB} (Σ_{DC}) [the black solid lines on the right-hand side of Figs. 6(b) and (d) are curling due to this spiral effect]. Therefore, the threshold $a = a_+^*$ between these two bifurcations is determined by the point at which \mathbf{X}_D^* changes between a node and a spiral. This is where the discriminant Q_{D-} of Eq. (30f) is 0. Solving an equation $Q_{D-} = 0$ for a , we obtain two solutions as

$$a = a_+^*, a_-^*, \quad (32)$$

where

$$a_+^* := \frac{\tau_y - \tau_x + 2\sqrt{b\tau_x\tau_y}}{\tau_y}, \quad (33a)$$

$$a_-^* := \frac{\tau_y - \tau_x - 2\sqrt{b\tau_x\tau_y}}{\tau_y}. \quad (33b)$$

The former satisfies $a_{\text{inf}} < a_+^* < 1 + b$, whereas the latter meets $0 < a_-^* < a_{\text{inf}}$. Thus, the threshold value a_+^* holds by (33a). The zenith of the dotted lines Δ_1 and Δ_2 on the vertical a -axis in Fig. 5 corresponds to $a = a_+^*$. Note that even if \mathbf{X}_D^* is a spiral, however, the system state which entered S_D crossing a boundary is not always destined to return to the same boundary. Suppose that the parameter condition is not in the neighborhood of $\partial\Omega_2^-$ and $\partial\Omega_3^-$, then \mathbf{X}_D^* can be separated from the two boundaries Σ_{BD} and Σ_{DC} . In this situation, it may be sufficient to bridge the system state from Σ_{BD} (Σ_{CD}) to the opposite side Σ_{DC} (Σ_{DB}), no matter how the spiral dynamics around \mathbf{X}_D^* work. The borderline of whether the stable limit cycle grazes the boundary Σ_{DC} (Σ_{DB}) and the

system state thereby successfully bridges to the opposite side, is represented as the dotted lines Δ_1 and Δ_2 shown in Fig. 5. At these borderlines, the oscillation type (d) and the others (a)–(c) are clearly separated, and the transition between them can be regarded as a grazing bifurcation¹⁸ of the limit cycle [Fig. 7(IV)].

C. Derivation of the Logarithmic Oscillation-Period Scaling Law

In Subsection III B, we discuss the limitations of the approximated oscillation period T_{harm} given by Eq. (18), which is previously proposed by Ref. 8. Instead of T_{harm} , we introduce a logarithmic scaling law T_{homo} as a more plausible approximation of oscillation period for larger asymmetric synaptic weights $a_{21} \neq a_{12}$ and asymmetric inputs given by $r \neq 1$:

$$T_{\text{homo}} := \tau_y \left[\ln \frac{1}{(1+b)a_{12}\delta^2} - \ln \frac{(r_{\text{sup}} - r)(r - r_{\text{inf}})}{r} \right], \quad (34)$$

where

$$\delta := \frac{\tau_y - \tau_x}{b\tau_y}. \quad (35)$$

These logarithmic forms of oscillation periods are commonly observed in the vicinity of homoclinic bifurcations.^{20,21} Figure 8 plots both the theoretical prediction T_{homo} by Eq. (34) and the actual oscillation period T along the cross-section (S2) as the horizontal dotted line drawn in Fig. 2, with the fixed value $a = 2.2$. The simplified version of Eq. (34) under $a = a_{12} = a_{21}$ and $r = 1$ is obtained as

$$T_{\text{homo}} = 2\tau_y \left[\ln \frac{1}{\delta} - \ln(1 + b - a) \right]. \quad (36)$$

The theoretical curve of Eq. (36) is illustrated by the solid lines in Fig. 3, which better agree with the actual oscillation period T (circle) than T_{harm} (dotted line). Note that even Eq. (34) cannot be applied to the oscillation type (d) shown in Fig. 6(d), which has a constant oscillation period for any r under fixed a_{12}, a_{21} .

To derive the scaling law T_{homo} of Eq. (34), we first divide an oscillation period T into four pieces corresponding to the separately colored trajectories in Fig. 6(a)–(c):

$$T = T_B + T_C + T_{D_1} + T_{D_2}, \quad (37)$$

where T_B , T_C , T_{D_1} , and T_{D_2} are the time durations required to pass through S_B , S_C , S_D from Σ_{BD} to Σ_{DC} , and S_D from Σ_{CD} to Σ_{DB} , respectively.

Next, we make several main assumptions.

Assumption 1. T_{D_1} and T_{D_2} can be ignored because these durations are shorter than T_B and T_C .

Assumption 2. The values of y_1 and y_2 remain almost unchanged while the system state passes the region S_D .

Assumption 3. The system state in the region S_B (or S_C) approaches \mathbf{X}_B^* (\mathbf{X}_C^*) along the slowest eigenvector \mathbf{v}_B (\mathbf{v}_C) corresponding to the eigenvalue $\lambda_B = -\frac{1}{\tau_y}$ ($\lambda_C = -\frac{1}{\tau_y}$).

Applying Assumption 1 to Eq. (37), we obtain

$$T \approx T_{\text{homo}} = T_B + T_C. \quad (38)$$

According to Eq. (28a), the dynamics in the region S_B are simply a first-order differential equation regarding y_2 :

$$\tau_y \frac{dy_2}{dt} = -y_2. \quad (39)$$

Hence, T_B is simply evaluated by the variation amount of y_2 as

$$T_B = \tau_y \ln \frac{[\mathbf{X}_B^0]_{y_2}}{[\mathbf{X}_B^1]_{y_2}}, \quad (40)$$

where \mathbf{X}_B^0 and \mathbf{X}_B^1 are the initial and terminal points of the passing trajectory in S_B , respectively. Similarly, y_1 follows the dynamics

$$\tau_y \frac{dy_1}{dt} = -y_1, \quad (41)$$

in the region S_C considering Eq. (29a). Therefore, T_C is given by

$$T_C = \tau_y \ln \frac{[\mathbf{X}_C^0]_{y_1}}{[\mathbf{X}_C^1]_{y_1}}, \quad (42)$$

where \mathbf{X}_C^0 and \mathbf{X}_C^1 are the start and end states of the oscillation path in the region S_C . Applying Assumption 2 results to the following approximation:

$$[\mathbf{X}_B^0]_{y_2} \approx [\mathbf{X}_C^1]_{y_2}, \quad (43a)$$

$$[\mathbf{X}_C^0]_{y_1} \approx [\mathbf{X}_B^1]_{y_1}. \quad (43b)$$

Now, the problem is reduced to calculating \mathbf{X}_B^1 and \mathbf{X}_C^1 . Considering Assumption 3, \mathbf{X}_B^1 is derived as an intersection between Σ_{BD} and the slowest eigenvector \mathbf{v}_B extended from the virtual

fixed point \mathbf{X}_B^* (this extension is roughly represented by the cyan dotted lines in Fig. 6). The eigenvector is

$$\mathbf{v}_B = \begin{bmatrix} 0 & 0 & 1 & -\delta \end{bmatrix}^\top. \quad (44)$$

Providing that $\mathbf{X}_B^1 = \mathbf{X}_B^* + k\mathbf{v}_B$, then $[\mathbf{X}_B^1]_{x_2} = 0$ when

$$k = -\frac{(1+b)r - a_{21}}{1+b} s_1. \quad (45)$$

Therefore, we can confirm

$$\mathbf{X}_B^1 = \begin{bmatrix} \frac{s_1}{1+b} & \frac{s_1}{1+b} & 0 & \frac{(1+b)r - a_{21}}{1+b} \delta s_1 \end{bmatrix}^\top. \quad (46a)$$

Similarly, we get

$$\mathbf{X}_C^1 = \begin{bmatrix} 0 & \frac{(1+b) - ra_{12}}{1+b} \delta s_1 & \frac{rs_1}{1+b} & \frac{rs_1}{1+b} \end{bmatrix}^\top. \quad (46b)$$

Considering Eqs. (43a), (43b), (46a), and (46b), Eqs. (40) and (42) are written as

$$T_B = \tau_y \ln \left(\frac{1}{\delta} \frac{r}{(1+b)r - a_{21}} \right), \quad (47a)$$

$$T_C = \tau_y \ln \left(\frac{1}{\delta} \frac{1}{(1+b) - ra_{12}} \right). \quad (47b)$$

Substituting Eqs. (47a) and (47b) into Eq. (38) and simplifying, the logarithmic scaling law of Eq. (34) holds.

The order of logarithmic divergence of T by Eq. (34) indicates a ghost in the oscillation type (c), which is close to the second homoclinic-like bifurcation. When (r, a) is close to the borderline $\partial\Omega_2^+$ (or $\partial\Omega_3^+$), the stable fixed point \mathbf{X}_B^* (\mathbf{X}_C^*) is still virtual, yet it is almost on Σ_{BD} (Σ_{CD}). Consequently, its saddle-like point effect causes a ghost, which requires a long duration to pass slowly. The orbit leading to this ghost point works as a bottleneck of time, which becomes dominant in the entire oscillation cycle.

Now we discuss the validity of the introduced approximations. Assumption 1 serves to eliminate oscillation patterns observed when a is small, such as the oscillation types (b) and (d). For oscillation types (a) and (c), this is a good approximation because the process of T_{D_1} and T_{D_2} is very fast. Assumption 2 brings an even coarser approximation. For example, along the lower black trajectories in the right of Fig. 6(c), which corresponds to the duration T_{D_2} of the oscillation type (c), the value of $Y = y_1 - y_2$ changes sufficiently that Assumption 2 may be inappropriate here. Another version of Eq. (34) without Assumption 2 is described in the Appendix.

Assumption 3 provides a good approximation, specifically for the oscillation type (c) slightly before the homoclinic-like bifurcation, where \mathbf{X}_B^* (or \mathbf{X}_C^*) is about to appear from the virtual state crossing the boundary Σ_{BD} (Σ_{CD}). For example, in Fig. 6(c), the direction of the trajectory in S_C (magenta solid line) in the vicinity of the virtual fixed point \mathbf{X}_C^* (magenta-edged circle) is almost identical to the slowest eigendirection of \mathbf{X}_C^* . Here, \mathbf{X}_C^* is positioned just before the boundary Σ_{CD} is crossed. This approximation is even worse for the oscillation type (b) shown in Fig. 6(b). According to the formulation in (28b) [or (29b)], the x_2 -coordinate of \mathbf{X}_B^* (x_1 -coordinate of \mathbf{X}_C^*) is expected to increase as a_{21} (a_{12}) decreases; the oscillation pattern approaches (b); thus, \mathbf{X}_B^* (\mathbf{X}_C^*) moves further away from Σ_{BD} (Σ_{CD}). According to the numerically simulated trajectories in Fig. 6, the longer distance between \mathbf{X}_B^* (\mathbf{X}_C^*) and Σ_{BD} (Σ_{CD}) is responsible for the inappropriate approximation by Assumption 3.

D. Noise-induced Oscillation

A novel result predicted regarding the second homoclinic-like bifurcation is that noise-induced oscillations emerge even through the parameter set (r, a_{12}, a_{21}) is on or slightly outside $\partial\Omega_2$ (or $\partial\Omega_3$). In this condition, the original noiseless system (1) only converges to the stable fixed point \mathbf{X}_B^* (\mathbf{X}_C^*) existing in the vicinity of Σ_{BD} (Σ_{CD}). This process is represented by the activity pattern of Fig. 1(f). To introduce external noise to the system, for example, we can replace Eq. (1a) by

$$\tau_x \frac{dx_i}{dt} = -x_i - by_i - \sum_{j \neq i}^n a_{ij} z_j + s_i + \sigma \eta, \quad (48)$$

where σ determines the noise intensity and η is the standard Gaussian noise.

If the noise intensity σ is sufficient, then the system state which almost converges to \mathbf{X}_B^* (\mathbf{X}_C^*) may by chance jump across Σ_{BD} (Σ_{CD}) into $S_D^* \subset S_D$. Here, S_D^* is a subregion in which there is a locally attracting homoclinic-like orbit inherited from the periodic orbits observed when (r, a_{12}, a_{21}) is inside $\partial\Omega_2$ ($\partial\Omega_3$). Nearly riding on this homoclinic-like orbit, the system state in turn starts an excursion through S_D , S_C , again S_D , and S_B [corresponding to the oscillation pattern (c)], or only through S_D and S_B [oscillation pattern (d)], returning to \mathbf{X}_B^* (\mathbf{X}_C^*). This is the overall dynamical picture of the noise-induced oscillations. Figure 9 shows examples of noise-induced oscillations observed in the vicinity of the homoclinic-like and supercritical Hopf-like bifurcations, the waveforms of which are inherited from the (c) and (d) oscillation patterns.

More practically, a noise-induced oscillation cycle can be defined as an itinerary that starts upon

crossing Σ_{BD} (Σ_{CD}) into S_D^* , undergoes a certain excursion returning to S_B (S_C), and terminates on crossing Σ_{BD} (Σ_{CD}) again. We can also define the oscillation period of a noise-induced oscillation as T_σ , which is the duration required for such a cycle. Here, T_σ is stochastically variable. When the noise is sufficiently small, the excursion process occupies only a small proportion of T_σ , and most of the remaining duration is allocated to the process of jumping from X_B^* (X_C^*) across Σ_{BD} (Σ_{CD}) into S_D^* which is driven by the external noise perturbations. This jumping duration is estimated as the minimum time spent to reach S_D^* and is expected to be shorter as the stochastic perturbation gets larger on average. In addition, X_B^* (X_C^*) separates further from Σ_{BD} (Σ_{CD}) as the parameter set (r, a_{12}, a_{21}) are distanced from the borderline $\partial\Omega_2$ or $\partial\Omega_3$. Under the same noise intensity σ , the duration required for the jumping process could increase as the jumping distance extends.

Thus, T_σ could increase as the noise intensity σ declines, or the parameter set (r, a_{12}, a_{21}) distances from the borderline $\partial\Omega_2$ or $\partial\Omega_3$. From another perspective, the divergence of T_σ is relieved and the oscillation-existing area Ω in the parameter space is widened, for a larger σ . These predictions can be numerically verified by evaluating the arithmetic mean of T_σ for multiple oscillation cycles (Fig. 10).

VI. DISCUSSION

This study's first step was the fixed point analysis of the two-neuron Matsuoka oscillator model (Section IV), which enabled a quantitative evaluation of transient neuronal activities as convergences to stable fixed points. We found that oscillatory solutions are caused by convergence to the virtual stable fixed points X_B^* and X_C^* and divergence from the existing unstable fixed point X_D^* (Subsection V A). This could be why the conditions for absence of the stable fixed points are equivalent to the existence condition of oscillations. Furthermore, this oscillation picture provided explanations of several bifurcation scenarios between oscillatory and stationary states, or between different oscillation types: subcritical Hopf-like, homoclinic-like, supercritical Hopf-like, and grazing bifurcations (Subsection V B). The additional knowledge presented in this paper such as the logarithmic oscillation-period scaling law (Subsection V C) and noise-induced oscillation (Subsection V D) were also obtained following the fixed point analysis in Section IV.

A. Mathematical Aspects

The logarithmic scaling law (34), as a new approximation T_{homo} for the oscillation period T , was derived in terms of the convergent linear dynamics of the variables y_1 and y_2 in the regions S_B and S_C . The order of the divergence of T_{homo} in this scaling law is similarly observed in the neighborhood of homoclinic bifurcations.^{20,21} However, the ‘‘homoclinic-like’’ bifurcation discussed in Subsection VB concerning this scaling law is slightly different from other homoclinic bifurcations. Standard homoclinic bifurcation has a saddle point approaching a limit cycle orbit. When these collide and fuse, the saddle point rides on the limit cycle orbit with the periodic oscillatory nature disappearing. Conversely, this model only has a virtual stable node \mathbf{X}_B^* (or \mathbf{X}_C^*) instead of a saddle point. At the homoclinic-like bifurcation moment, \mathbf{X}_B^* (\mathbf{X}_C^*) reaches the boundary Σ_{BD} (Σ_{CD}) and transforms from a virtual into a regular state. Because oscillations are caused by convergence to virtual \mathbf{X}_B^* (\mathbf{X}_C^*), at this homoclinic-like bifurcation, it naturally emerges on the original periodic orbit. Moreover, in this situation, the dynamics flow into the \mathbf{X}_B^* (\mathbf{X}_C^*) from the region S_B (S_C) and escape to S_D , which made \mathbf{X}_B^* (\mathbf{X}_C^*) assume a saddle-like property.

Beyond this bifurcation, \mathbf{X}_B^* (\mathbf{X}_C^*) distances from Σ_{BD} (Σ_{CD}). Even in this situation, an oscillatory excursion along the homoclinic-like orbit could occur if a sufficient perturbation is adopted to cross over that gap. This is the noise-induced oscillation proposed in Subection VD, which is essentially common to phenomena described as ‘‘noise-invoked resonance,’’ for instance, in previous studies concerning homoclinic bifurcations.^{21,22} It is plausible that as biological systems, neural circuits are always influenced by noise. Therefore, the results concerning the noise-induced oscillation in the present study would provide a foundation for validating CPG models through biological experiments.

Unlike the logarithmic approximation T_{homo} , the previously proposed approximation T_{harm} given by Eq. (18) was derived in terms of an approximation of a periodic cycle into a behavior of the harmonic oscillator in the region S_D . In particular, at $\partial\Omega_1$, this approximation is strictly accurate because the oscillation pattern becomes neutrally stable around a center, \mathbf{X}_D^* . This change in the stability of \mathbf{X}_D^* is responsible for the subcritical Hopf-like bifurcation in the vicinity of the borderline $\partial\Omega_1$. There remains the problem that the previous approximation T_{harm} is valid only in the symmetric network $a = a_{12} = a_{21}$ and not applicable to asymmetric cases $a_{12} \neq a_{21}$ like the new approximation T_{homo} . Hence, it is a future prospect to modify T_{harm} given by Eq. (18) into more general formulation which also covers asymmetric cases. This approach may be even

essential to answer another question of why the oscillation type (d) has an invariant oscillation period independent of the value of r .

The oscillation types (c) and (d) were found by eliminating the assumption of symmetry input stimuli into the two neurons ($r = 1$), which has been adopted in many previous studies. For example, Ref. 23 investigated the stability of a limit-cycle solution in the symmetric $r = 1$ case of the two-neuron Matsuoka oscillator model. Because the stability of the oscillation types (c) and (d) was only numerically confirmed in this paper and not theoretically guaranteed, a future undertaking is to resolve this problem by extending the method of impact maps described in Ref. 23.

B. Biological Interpretations and Limitations

The external inputs into neurons s_1 and s_2 were set as constants throughout this study. Suppose that values of the synaptic weights a_{12} and a_{21} are fixed to satisfy Ineq. (9), the input ratio $r = \frac{s_2}{s_1}$ is the only bifurcation parameter between stable stationary states and stable oscillations. Gradual and continuous incrementation of r is equal to alterations along the horizontal axis like (S2) in Fig. 2, which contributes to phase transition among

- convergent dynamics to \mathbf{X}_B^* when (28d),
- oscillatory dynamics under the condition (30m), and
- convergent dynamics to \mathbf{X}_C^* if (29d) is true.

In this sense, \mathbf{X}_B^* or \mathbf{X}_C^* are supposed to be the start or end points of transient neuronal activities. This could be a hypothesis for the continuous transition between oscillatory and convergent neuronal activities, and even between rhythmic and discrete movements.

The present analysis suggests that the Matsuoka oscillator model has the restriction that \mathbf{X}_D^* cannot be a stable fixed point when the values of the synaptic weights a_{12} , a_{21} are fixed to satisfy the existence condition of oscillatory solutions (9). Two coupled neurons of the Matsuoka oscillator model have been used to model the flexion and extension of a single joint by matching each neuron to either a flexor or extensor muscle.¹⁶ In this situation, however, it is impossible to achieve the stationary states where the two neurons are simultaneously activated leading to stationary co-contraction of the muscles. To reproduce this sustainable co-activation of neurons with the original Matsuoka oscillator model, synaptic weights a_{12} and a_{21} should change as fast as the ratio

of inputs into the neurons $r = \frac{s_2}{s_1}$. One possible scheme is to assume specific interneurons between the two main neurons. Parameters a_{12} and a_{21} are regarded as the overall transmission efficiency between the two main neurons, mediated by the interneurons, the values of which are regulated by other external input signals imposed on the interneurons. This structure should involve a time delay in the process of multiple synaptic transmissions, although this is not assumed in the original Matsuoka oscillator model. Improving the original model into a more plausible one that is consistent with physiological findings on neurons and neuronal networks will be an important future development.

Finally, the analysis of the Matsuoka oscillator model in this study was consistently limited to the two-neuron case. When the number of neurons is $n \geq 3$, the network topologies become more complex and analysis is harder because it requires the solving of sixth- or higher-order equations. However, the fixed point analysis in this study may be useful in understanding the properties of the multi-neuron dynamical system. Because there are n variables of the membrane potential x_i ($i = 1, 2, \dots, n$), the solution space is divided into 2^n regions regarding the positivity or negativity of x_i . Thus, we could investigate the dynamics specific to each region, the fixed points in the relevant dynamics, and the existence and stability of the fixed points. Extending the present results to the general n -neuron version of the Matsuoka oscillator model may be necessary to understand CPG circuits in the spinal cord as a huge multidimensional system.

ACKNOWLEDGMENTS

We thank the lab members in Nonlinear Physics Group (Kori-Kobayashi-Izumida Group) and peers in The Japanese Society for Motor Control and The Society for the Neural Control of Movement, for research discussion and constructive criticism. This study was supported by JSPS KAKENHI (No. JP24KJ0876) and Scholarship for Graduate Students by Nakatani Foundation for Advancement of Measuring Technologies in Biomedical Engineering to K.M., and JSPS KAKENHI (No. JP21J10799, JP23H02796) to H.K.

AUTHOR DECLARATIONS

Conflict of Interest

The authors have no conflicts to disclose.

Author Contributions

K.M and H.K. conceived the project. K.M. performed theoretical and numerical analysis. K.M. wrote the manuscript under the supervision by H.K.

DATA AVAILABILITY STATEMENT

The data that support the findings of this study are available within the article [and its supplementary material].

Appendix: Revised Version of the Logarithmic Oscillation-Period Scaling Law

Instead of Assumption 2, a new one could be introduced;

Assumption 4. The values of y_1 and y_2 change along the fastest eigenvector \mathbf{v}_D of the unstable fixed point \mathbf{X}_D^* in region S_D .

This can be available only when \mathbf{X}_D^* is an unstable node, not an unstable spiral, which occurs under the $a \geq a_+^*$ condition. Additionally, Assumption 4 is consistent with Assumption 1; thus, the oscillation types (a) and (c) also serve for good approximation by Assumption 4 because under this condition, the diverging effect of the slower eigenvector reduces throughout T_{D_1} and T_{D_2} . The fastest eigenvector \mathbf{v}_D is

$$\mathbf{v}_D = \begin{bmatrix} 1 & v & -\alpha & -\alpha v \end{bmatrix}^\top, \quad (\text{A.1})$$

where

$$\alpha = \sqrt{\frac{a_{21}}{a_{12}}}, \quad (\text{A.2})$$

$$v = \frac{\tau_x - (1 - \sqrt{a_{12}a_{21}})\tau_y - \sqrt{Q_{D-}}}{2b\tau_y}. \quad (\text{A.3})$$

Note that Q_{D-} is the discriminant of Eq. (30f). Instead of Eqs. (43a) and (43b), Assumption 4 leads to

$$\mathbf{X}_B^0 = \mathbf{X}_C^1 + k_B \mathbf{v}_D, \quad (\text{A.4a})$$

$$\mathbf{X}_C^0 = \mathbf{X}_B^1 + k_C \mathbf{v}_D. \quad (\text{A.4b})$$

Solving $[\mathbf{X}_B^0]_{x_2} = 0$ and $[\mathbf{X}_C^0]_{x_1} = 0$, we obtain

$$k_B = \frac{rs_1}{\alpha(1+b)}, \quad (\text{A.5a})$$

$$k_C = -\frac{s_1}{1+b}, \quad (\text{A.5b})$$

which is followed by

$$[\mathbf{X}_B^0]_{y_2} = (1-\nu) \frac{rs_1}{1+b}, \quad (\text{A.6a})$$

$$[\mathbf{X}_C^0]_{y_1} = (1-\nu) \frac{s_1}{1+b}. \quad (\text{A.6b})$$

Substituting Eqs. (46a), (46b), (A.6a), and (A.6b) into Eqs. (40) and (42), we get

$$T_B = \tau_y \ln \left(\frac{1}{\delta} \frac{(1-\nu)r}{(1+b)r - a_{21}} \right), \quad (\text{A.7a})$$

$$T_C = \tau_y \ln \left(\frac{1}{\delta} \frac{(1-\nu)1}{(1+b) - ra_{12}} \right). \quad (\text{A.7b})$$

Finally, in applying Eqs. (A.7a) and (A.7b) to Eq. (38), the following result holds:

$$T_{\text{homo}}^* = \tau_y \left[\ln \frac{(1-\nu)^2}{(1+b)a_{12}\delta^2} - \ln \frac{(r_{\text{sup}} - r)(r - r_{\text{inf}})}{r} \right]. \quad (\text{A.8})$$

This is the revised version of the oscillation-period scaling law. Compared with the original version, T_{homo} , given by (34), this form T_{homo}^* differs only in the constant term for the coefficient $(1-\nu)^2$ in the logarithm. Figure 11 shows the curve of T_{homo}^* in the same form as Figs. 3 and 8. Here, $T_{\text{homo}}^* \leq T_{\text{homo}}$ holds so that T_{homo}^* seems less accurate than T_{homo} for the numerically observed oscillation period T . This is because the duration T_D is ignored according to Assumption 1. If T_D is accurately reckoned, then T_{homo}^* will be closer to T than T_{homo} .

REFERENCES

- ¹A. J. Ijspeert, A. Crespi, D. Ryczko, and J.-M. Cabelguen, ‘‘From swimming to walking with a salamander robot driven by a spinal cord model,’’ *science* **315**, 1416–1420 (2007).
- ²A. J. Ijspeert, ‘‘Central pattern generators for locomotion control in animals and robots: a review,’’ *Neural networks* **21**, 642–653 (2008).
- ³S. Grillner, ‘‘Biological pattern generation: the cellular and computational logic of networks in motion,’’ *Neuron* **52**, 751–766 (2006).

- ⁴T. Takei and K. Seki, “Spinal premotor interneurons mediate dynamic and static motor commands for precision grip in monkeys,” *Journal of Neuroscience* **33**, 8850–8860 (2013).
- ⁵E. Azim, J. Jiang, B. Alstermark, and T. M. Jessell, “Skilled reaching relies on a v2a propriospinal internal copy circuit,” *Nature* **508**, 357–363 (2014).
- ⁶K. Matsuoka, “Sustained oscillations generated by mutually inhibiting neurons with adaptation,” *Biological cybernetics* **52**, 367–376 (1985).
- ⁷K. Matsuoka, “Mechanisms of frequency and pattern control in the neural rhythm generators,” *Biological cybernetics* **56**, 345–353 (1987).
- ⁸K. Matsuoka, “Analysis of a neural oscillator,” *Biological cybernetics* **104**, 297–304 (2011).
- ⁹E. Angelidis, E. Buchholz, J. Arreguit, A. Rougé, T. Stewart, A. von Arnim, A. Knoll, and A. Ijspeert, “A spiking central pattern generator for the control of a simulated lamprey robot running on spinnaker and loihi neuromorphic boards,” *Neuromorphic Computing and Engineering* **1**, 014005 (2021).
- ¹⁰G. Taga, Y. Yamaguchi, and H. Shimizu, “Self-organized control of bipedal locomotion by neural oscillators in unpredictable environment,” *Biological cybernetics* **65**, 147–159 (1991).
- ¹¹G. Taga, “A model of the neuro-musculo-skeletal system for human locomotion: I. emergence of basic gait,” *Biological cybernetics* **73**, 97–111 (1995).
- ¹²N. Ogihara and N. Yamazaki, “Generation of human bipedal locomotion by a bio-mimetic neuro-musculo-skeletal model,” *Biological cybernetics* **84**, 1–11 (2001).
- ¹³H. R. Wilson and J. D. Cowan, “Excitatory and inhibitory interactions in localized populations of model neurons,” *Biophysical journal* **12**, 1–24 (1972).
- ¹⁴H. R. Wilson and J. D. Cowan, “A mathematical theory of the functional dynamics of cortical and thalamic nervous tissue,” *Kybernetik* **13**, 55–80 (1973).
- ¹⁵S. Degallier and A. Ijspeert, “Modeling discrete and rhythmic movements through motor primitives: a review,” *Biological cybernetics* **103**, 319–338 (2010).
- ¹⁶A. de Rugy and D. Sternad, “Interaction between discrete and rhythmic movements: reaction time and phase of discrete movement initiation during oscillatory movements,” *Brain Research* **994**, 160–174 (2003).
- ¹⁷S. H. Strogatz, “Nonlinear dynamics and chaos: With applications to physics, biology,” *Chemistry and Engineering* **441** (1994).
- ¹⁸M. Di Bernardo, C. J. Budd, A. R. Champneys, P. Kowalczyk, A. B. Nordmark, G. O. Tost, and P. T. Piiroinen, “Bifurcations in nonsmooth dynamical systems,” *SIAM review* **50**, 629–701

- (2008).
- ¹⁹M. Bernardo, C. Budd, A. R. Champneys, and P. Kowalczyk, *Piecewise-smooth dynamical systems: theory and applications*, Vol. 163 (Springer Science & Business Media, 2008).
 - ²⁰P. Gaspard, “Measurement of the instability rate of a far-from-equilibrium steady state at an infinite period bifurcation,” *Journal of Physical Chemistry* **94**, 1–3 (1990).
 - ²¹G. J. E. Santos, M. Rivera, M. Eiswirth, and P. Parmananda, “Effects of noise near a homoclinic bifurcation in an electrochemical system,” *Physical Review E* **70**, 021103 (2004).
 - ²²M. Nurujjaman, A. S. Iyengar, and P. Parmananda, “Noise-invoked resonances near a homoclinic bifurcation in the glow discharge plasma,” *Physical Review E* **78**, 026406 (2008).
 - ²³J. M. Gonçalves, “Regions of stability for limit cycle oscillations in piecewise linear systems,” *IEEE Transactions on Automatic Control* **50**, 1877–1882 (2005).
 - ²⁴N. Hogan and D. Sternad, “On rhythmic and discrete movements: reflections, definitions and implications for motor control,” *Experimental brain research* **181**, 13–30 (2007).
 - ²⁵T. Flash and N. Hogan, “The coordination of arm movements: an experimentally confirmed mathematical model,” *Journal of neuroscience* **5**, 1688–1703 (1985).
 - ²⁶Y. Uno, M. Kawato, and R. Suzuki, “Formation and control of optimal trajectory in human multijoint arm movement,” *Biological cybernetics* **61**, 89–101 (1989).
 - ²⁷E. Todorov and M. I. Jordan, “Optimal feedback control as a theory of motor coordination,” *Nature neuroscience* **5**, 1226–1235 (2002).
 - ²⁸T. Ikegami, M. Hirashima, G. Taga, and D. Nozaki, “Asymmetric transfer of visuomotor learning between discrete and rhythmic movements,” *Journal of Neuroscience* **30**, 4515–4521 (2010).
 - ²⁹A. d’Avella, P. Saltiel, and E. Bizzi, “Combinations of muscle synergies in the construction of a natural motor behavior,” *Nature neuroscience* **6**, 300–308 (2003).
 - ³⁰T. Takei, J. Confais, S. Tomatsu, T. Oya, and K. Seki, “Neural basis for hand muscle synergies in the primate spinal cord,” *Proceedings of the National Academy of Sciences* **114**, 8643–8648 (2017).
 - ³¹S. Degallier, L. Righetti, S. Gay, and A. Ijspeert, “Toward simple control for complex, autonomous robotic applications: combining discrete and rhythmic motor primitives,” *Autonomous robots* **31**, 155–181 (2011).
 - ³²S. Schuster and M. Marhl, “Bifurcation analysis of calcium oscillations: time-scale separation, canards, and frequency lowering,” *Journal of Biological Systems* **9**, 291–314 (2001).

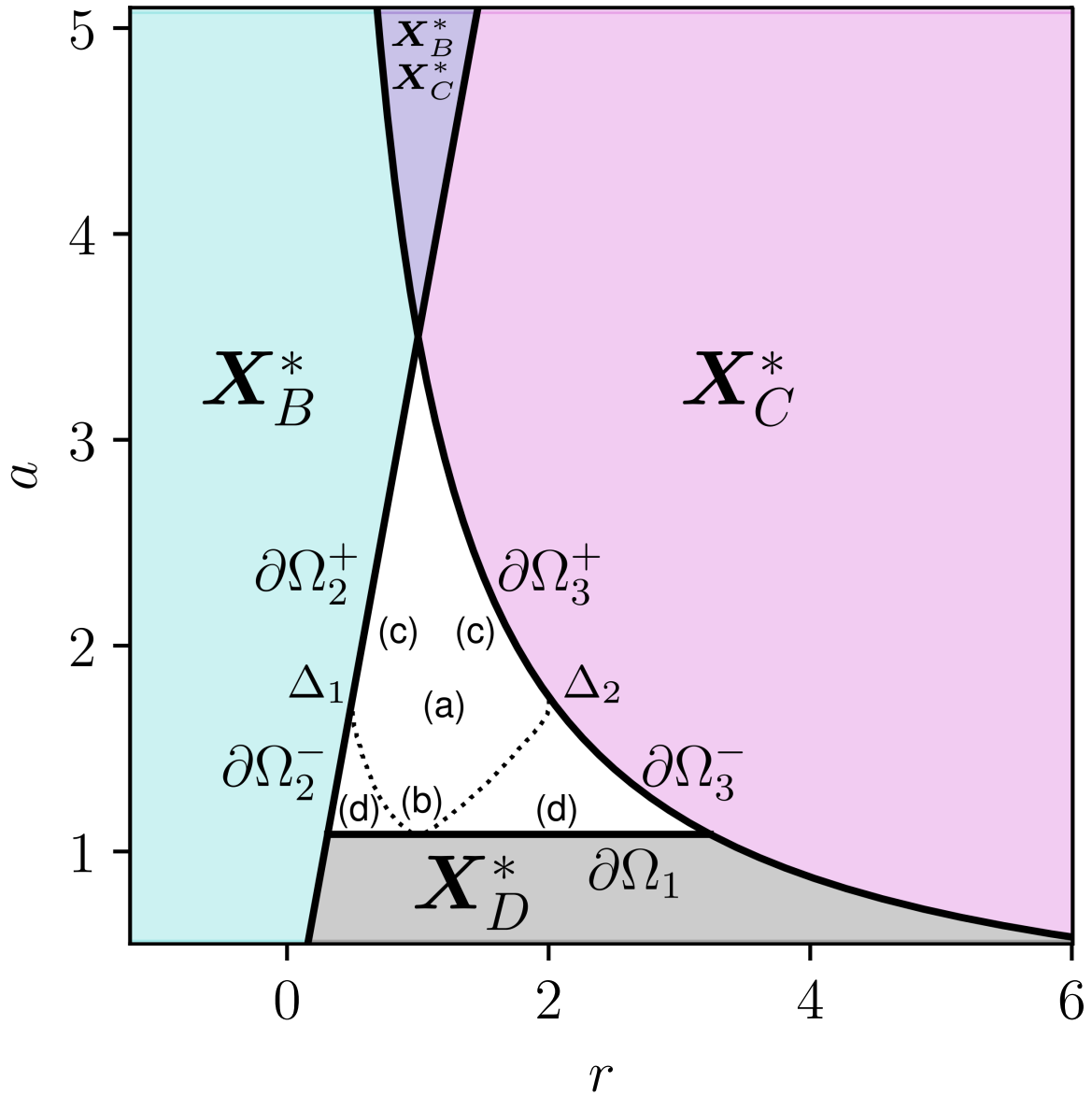


Fig. 5. Phase diagram of the same r - a plane as in Fig. 2. Stable oscillations emerge in Ω (white) surrounded by the borderlines $\partial\Omega_1$, $\partial\Omega_2$, and $\partial\Omega_3$ (black solid lines). The notations (a)–(d) express the rough locations where the corresponding oscillation types (a)–(d) are observed. Note that the oscillation type (d) non-smoothly transits to the other oscillation types (a)–(c) at the Δ_1 and Δ_2 borderlines (dotted line).

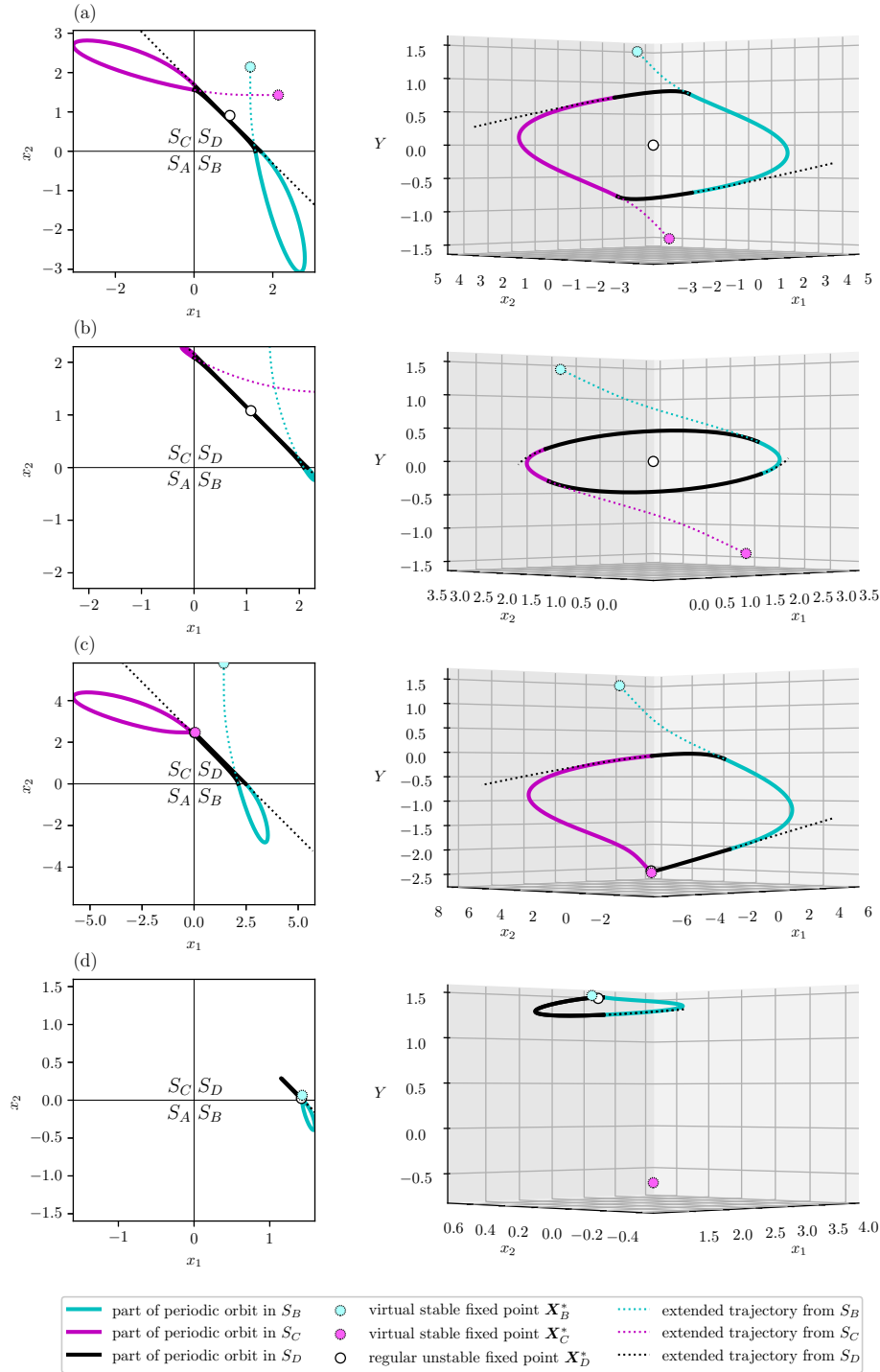


Fig. 6. Trajectories of oscillation patterns of Fig. 1(a)–(d) plotted on the x_1 - x_2 plane (left column) and the x_1 - x_2 - Y space (left column, for $Y = y_1 - y_2$). The system dynamics switch at Σ_{BD} (positive part of the x_1 -axis) and Σ_{CD} (positive part of the x_2 -axis), where the color of the periodic orbit (solid line) changes. For $i \in \{B, C, D\}$, the “extended trajectory from S_i ” (dotted line) would be hypothetically realized if the dynamics in the region S_i continued to operate after the system state escaped from S_i .

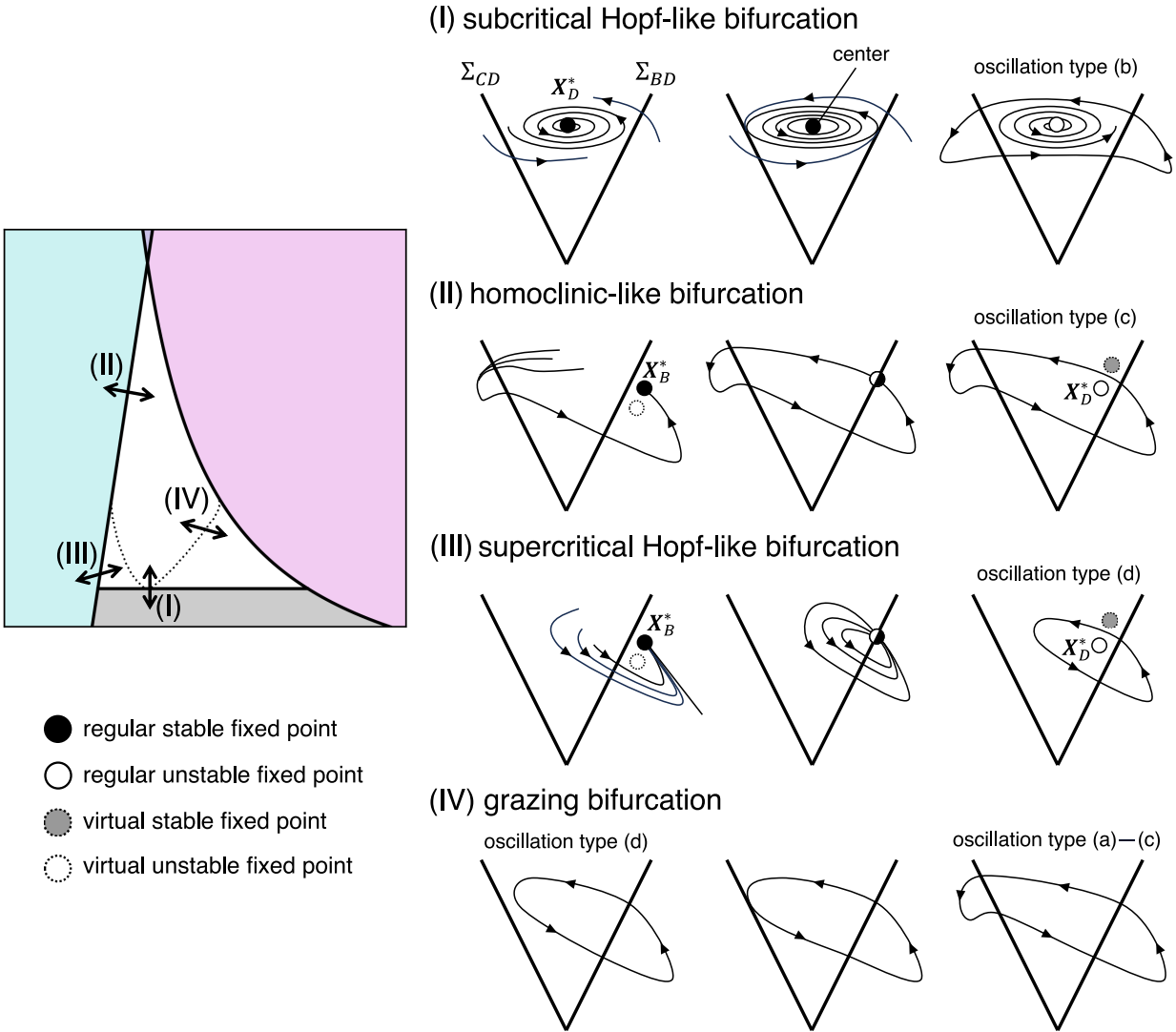


Fig. 7. Schematic diagram of the discontinuity-induced bifurcation scenarios. The bifurcations (I)–(IV) in the right-hand side are observed when parameter set (r, a) changes crossing the borderlines $\partial\Omega_1$, $\partial\Omega_2$, or $\partial\Omega_1$, and Δ_1 or Δ_2 as shown in the left-hand side, which is the same phase diagram as Fig. 5. In general, the periodic cycle generated through the subcritical Hopf-like bifurcation (I) is of both the oscillation types (b) and (d). In the bifurcation point of (I), the fixed point X_D^* is a center. Although there are other regular and virtual fixed points in the bifurcations (I) and (IV), which are not directly related to the bifurcation scenarios, are omitted for simplicity.

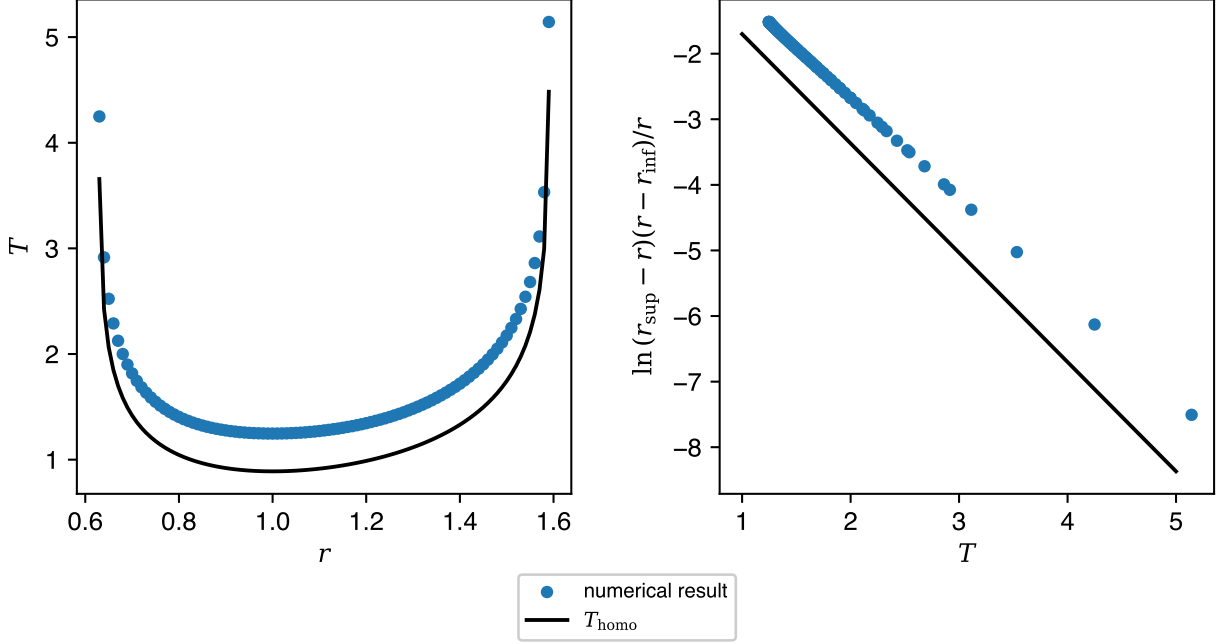


Fig. 8. (Left) Plot of the oscillation period T vs the symmetric synaptic weight a with fixed value $a = 2.2$ corresponding to the dotted line (S2) in Fig. (2). (Right) Another plot version of $\ln(r_{\text{sup}} - r)(r - r_{\text{inf}})/r$ vs the oscillation period T .

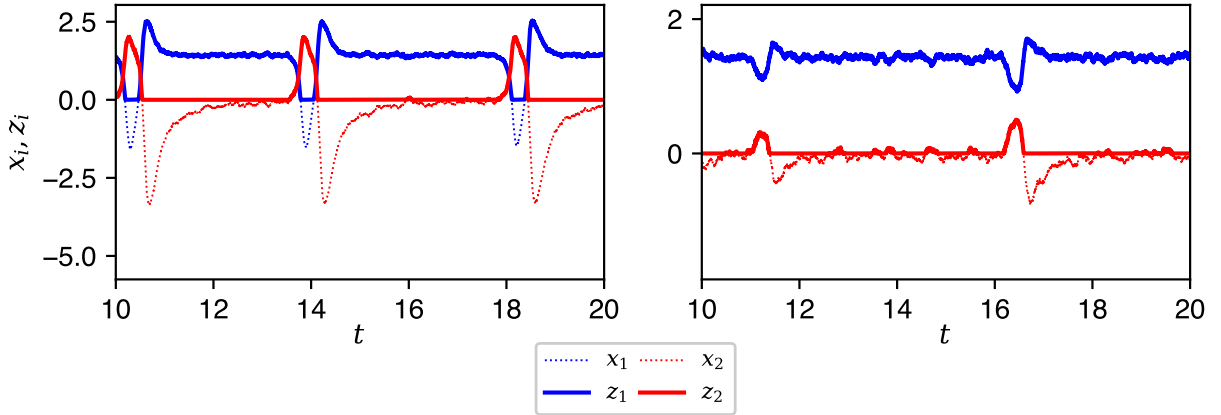


Fig. 9. Neuronal activity patterns observed in the noisy system (5) with Eq. (5a) replaced by Eq. (48), where $\sigma = 0.2$ and $a = a_{12} = a_{21}$; (Left) $a = 2$, $r = 0.56$, which is the same condition as Fig. 1(f). Similar to oscillation type (c). (Right) $a = 1.6$, $r = 0.455$. Similar to oscillation type (d).

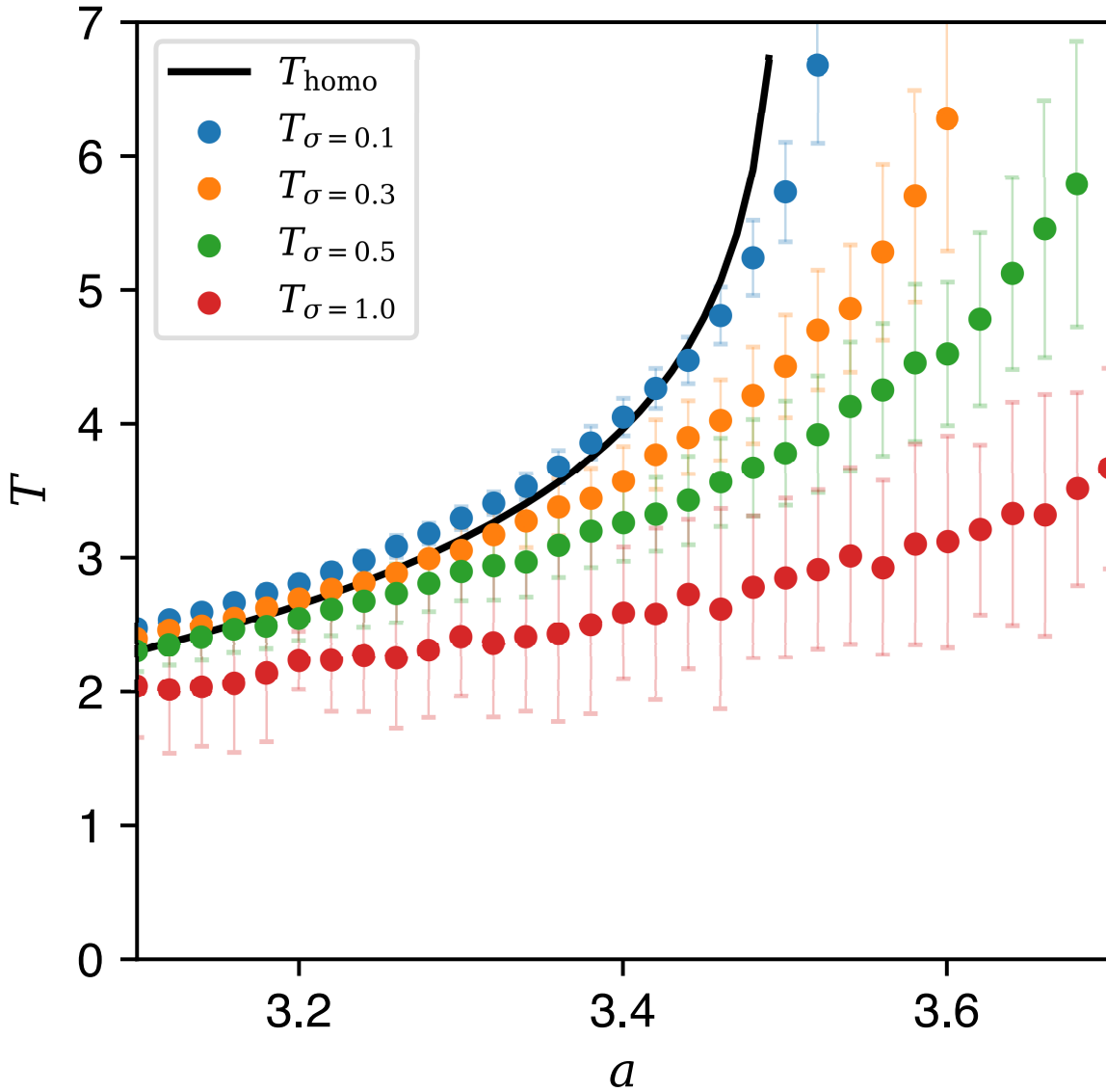


Fig. 10. Plot of average periods T_σ of noise-induced oscillations for various σ and $a = a_{12} = a_{21}$ under the condition $r = 1$, with the plot of T_{homo} (black) in Fig. 3. Each circle plot is calculated by averaging the periods of 200 numerically simulated noise-induced oscillation cycles, with error bars of their standard deviations.

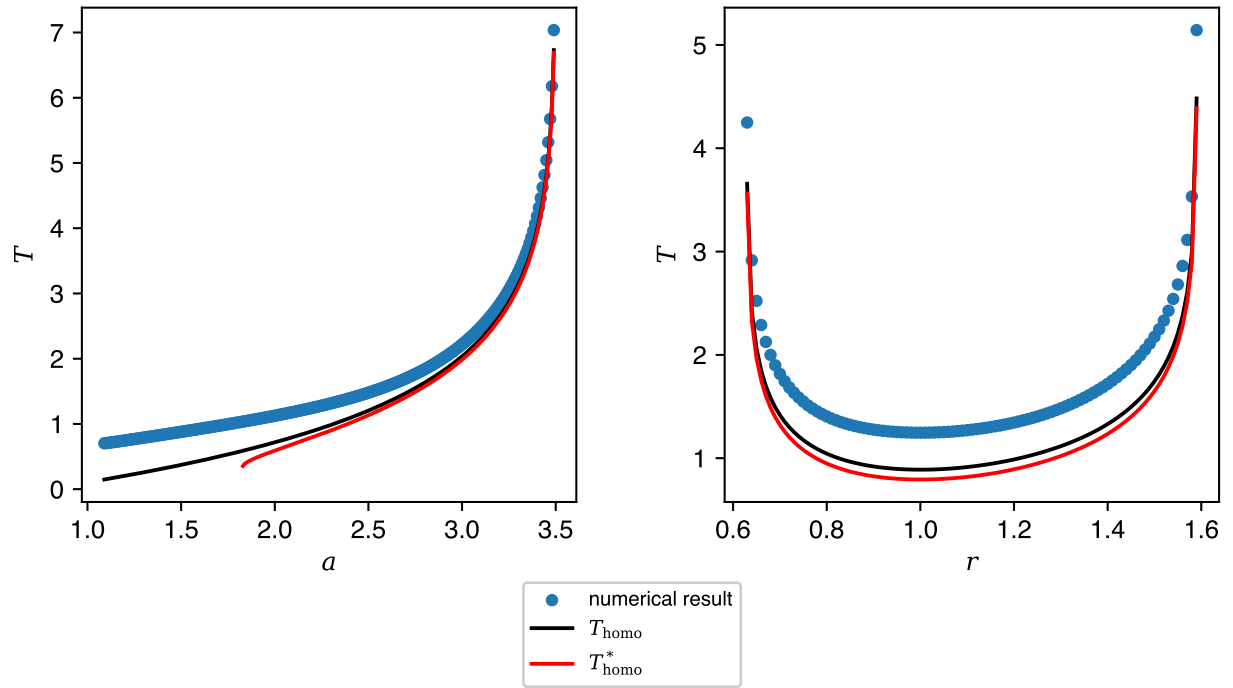


Fig. 11. The curves of the revised version T_{homo}^* are added to the left-hand side of Fig. 3 (Left), and the left-hand side of Fig. 8 (Right). Note that T_{homo}^* is only defined in the $a \geq a_+^*$ region.